MASTER

Investigation of the determination of optical properties with the use of integrating spheres and an inverse adding doubling algorithm

Baselmans, J.

Award date:
1993

UNIVERSITY OF TECHNOLOGY EINDHOVEN, THE NETHERLANDS

Technische Universiteit Eindhoven
Faculteit der Technische Natuurkunde
Vakgroep: Analyse van Fysische Meetmethoden

LASER CENTRE OF THE ACADEMIC MEDICAL CENTRE IN AMSTERDAM
PHILIPS RESEARCH LABORATORIES IN EINDHOVEN

INVESTIGATION OF THE DETERMINATION OF OPTICAL PROPERTIES WITH THE USE OF INTEGRATING SPHERES AND AN INVERSE ADDING DOUBLING ALGORITHM

Jan Baselmans

Afstudeerwerk verricht op het
Laser Centrum van het Academisch Medisch Centrum te Amsterdam
en op het
Philips Natuurkundig Laboratorium te Eindhoven.

Abstract

The determination of optical properties: probability for absorption (μ_a) and scattering (μ_s) and the anisotropy after scattering (g) of turbid media, with the use of integrating spheres, has been investigated. This is done by Monte Carlo simulations and integrating sphere measurements. One optical property was also determined with a time resolved technique. Both measurement techniques are compared with each other and with theoretical derived optical properties. (Mie theory) This all was done to understand a thickness dependence of two optical properties found by others. All the optical theories used are described: Mie theory, Radiative transfer, Monte Carlo simulations, Adding Doubling and time dependent diffusion theory. Furthermore a description of the measurement technique: Integrating spheres, is given.

From simulations it followed that the light distribution coming from a sample is not equally distributed over all angles (non-Lambertian) and that losses appear within the integrating spheres to the sides of the sample, which is placed against, or in between, integrating spheres. The measurements were done with to phantoms: polystyrene and Intralipid$^{®}$ of different concentrations and different sample thicknesses. The polystyrene measurements were in agreement with Mie theory, for both measurement techniques. The Intralipid measurements agreed within the both measurement techniques and was found to be: $\mu_{so} = 40 \pm 4$ cm^{-1} %$^{-1}$, g = 0.66 $\pm$ 0.02 at 633 nm and $\mu_{so} = 23 \pm 2$ cm^{-1} %$^{-1}$, g = 0.52 $\pm$ 0.03 at 780 nm, for the integrating sphere measurement.

From measurements and simulations it followed that it is not possible to measure low absorption coefficients within integrating spheres, because the absorption coefficient determined is largely caused by losses within the integrating spheres. For these losses can not be accounted for, because they depend on the optical properties themselves.

Contents

III

Table I: List of the most used symbols.

*Vectors are printed **bold**, unity vectors are printed with a ^-sign above. Subscripts are used to distinguish between the different media, superscripts are used to distinguish between old and new parameters.*

Symbol:	Description:
General:	
λ	Wavelength. [m]
$\varnothing$	Diameter. [m]
d	Thickness of the turbid medium. [m]
t	Time. [s]
c	Speed of light in a medium. [m s^{-1}]
$\hat{s}$	Unity vector in the direction of propagation. [sr^{-1}]
$\hat{n}$	Normal vector. [-]
θ, ϕ	Angles with the cartesian z- and x-axis. [rad]
$d\hat{s}$, $\sin\theta\ d\theta\ d\phi$	Solid integration angle. [sr]

Optical properties:	
$\sigma_s, \sigma_a, \sigma_t, \sigma_{pr}$	Cross sections for scattering, absorption, total attenuation and removed momentum. [m^2]
μ_s, μ_a, μ_t	Scattering, absorption and total attenuation coefficient. [m^{-1}]
g, a, τ	Anisotropic factor, albedo and optical thickness. [-]
$\mu_s' = \mu_s\ (1-g)$	The effective scattering coefficient. [m^{-1}]
$p(\hat{s},\hat{s}')$	(Single scattering) phase function. [sr^{-1}]
n	Index of refraction. [-]
$L(\mathbf{r},\hat{s},t)$	Radiance. [W m^{-2} sr^{-1}]
$\phi(\mathbf{r},t)$	(Radiant energy) fluence rate. [W m^{-2}]
$\mathbf{F}(\mathbf{r},t)$	Net flux. [W m^{-2} sr^{-1}]
$\Gamma(\zeta,t)$	Output flux. [W m^{-2} s^{-1}]

Monte Carlo	
P( )	Probability function. $[?^{-1}]$
ξ	Random number uniform distributed between 0 and 1. [-]
R	Reflection coefficient. [-]
$r = (x,y,z)$	Spatial coordinates. [m]
(u,v,w)	Direction of propagation. [-]
l	Step size. [m]
W	Propagation weight. [J]

Integrating sphere	
s, δ, h	Area sample port, detector port and holes. [cm]
A	Total inner sphere area (inclusive all ports). [cm]
α	Relative inner sphere area (exclusive all ports). [-]
β	Efficiency of detection. [-]
P, P_d	Incident and detected power. [W]
m	Coefficient of reflection of the sphere wall. [-]
R_d, T_d	Diffuse reflection and transmission factors of the sample with diffuse incident light. [-]
R_{cd}, T_{cd}	Collimated reflection and transmission factors of the sample with diffuse incident light. [-]
T_c, R_c	Collimated reflection and transmission factors of the sample with collimated incident light. [-]
K	Efficiency of the detector [V] *or* [A] *depending on the detector used.*
B_1, B_2	Sphere constants. [V] *or* [A] *respectively* [-] (B_1 *has the same dimension as* K.)
$V_\%$	Detected power. [V]
r_s	Radius sample port. [m]

V

1. Introduction

Lasers are widely used in medicine. Many different lasers are used for different applications based on the various laser-tissue interactions. For instance the treatment of port wine stains [27] is based on the selective absorption of laser light by blood which causes irreversible damage to the blood vessels. To optimize this therapy one has to choose the laser wavelength, spot size, power and pulse duration. This has to be done in such a way that only the target vessel is damaged and the rest of the skin remains intact. For this therapy (and many others) the light distribution within the tissue has to be known. This distribution depends on the optical properties of the tissue.

The optical properties can be measured in various ways. Here optical properties are are experimentally investigated with integrating spheres and time resolved measurements. For both measurements the same concentrations of polystyrene and Intralipid® are used. The measurements are done in order to understand a thickness-dependence of the optical properties found by others [2] [28], and are compared with Monte Carlo simulations and Mie theory.

With the integrating spheres the optical properties are derived in an indirect way. The diffuse reflected and transmitted light intensities, of a thin sample, are measured. The relation, between power detected within an integrating sphere and reflection and transmission coefficients of a sample, is derived by signal flow graphs and Mason's rule [15] (chapter 3). An Inverse Adding Doubling algorithm, is used to reconstruct the optical properties from the integrating sphere measurement.

Time dependent diffusion theory is used to calculate the optical properties from the time resolved measurement.

Monte Carlo simulations, Adding Doubling and time dependent diffusion theory are implementations of radiative transfer theory. This theory describes light propagation through turbid media by a conservation law. Mie theory describes light scattering by one spherical particle, with the use of Maxwell equations.

Finally a discussion of the methods used will be given (chapter 6) and some concluding remarks (chapter 7) on the measurement of optical properties with the use of integrating spheres will end this report.

2. Light transport

2.1 Introduction

Tissue optics is determined by the optical properties of tissue (absorption, scattering and angular distribution after scattering). It can be described by the Maxwell equations [11]. Solutions of the Maxwell equations are only known in simple geometries. A simple geometry for scattering is one sphere in a homogeneous medium, with a different index of refraction. This geometry was described by Gustav Mie (section 2.2).

In tissue, however, the propagation of light is characterized by multiple reflections and multiple refractions of light. This is caused by differences in index of refraction on the scale of the wavelength. So instead of solving the Maxwell equations for such a complex (random) medium, radiative transfer can be used to describe the propagation of light through tissue (section 2.4). This theory is based on bulk optical properties of tissue (section 2.3) and neglects the wave-like phenomena of light.

There are several methods and approximations to deal with the equation of radiative transfer. We used Monte Carlo simulations, Adding Doubling and time dependant diffusion theory. Monte Carlo simulations (section 2.5) are commonly used to visualize light energy distributions within tissue. Monte Carlo simulations are able to deal with complex geometries, but they are very time-consuming. In case of a plane parallel structure Adding Doubling (section 2.6) can be used for solving the transport equation. Adding Doubling calculates an angular distribution of the reflected and transmitted light of a slab of given thickness. Due to the geometry used, results are achieved independent of the spatial coordinates. Adding Doubling is relatively fast and any desired accuracy can be achieved. This makes it very useful for inverse procedures, where the optical properties need to be solved from e.g. transmission and reflection data. Time dependent diffusion theory (section 2.7) is used to derive optical properties from time resolved measurements. Diffusion theory is an approximation of radiative transfer theory. The angular distribution of the light radiance is developed as a multipole and only its first two moments are considered. In this way, the radiative transfer equation goes over into the diffusion equation which can be solved analytically. This means that solutions can be calculated in a very fast way. In view of the approximations used, the application of diffusion theory thereby remains to be seen.

2.2 Mie theory

The description of the scattering of a plane electromagnetic wave by a spherical particle that was given by Mie [13] is exact, since it is the solution of Maxwell's equations in a spherical geometry. It gives the cross sections for scattering σ_s, extinction σ_t and momentum removed σ_{pr}, for a given particle diameter ϕ, wavelength λ and relative index of refraction n. The wavelength is the wavelength of the light in the surrounding medium. The relative index of refraction is the index of refraction of the sphere divided by the index of refraction of the surrounding medium. The cross sections are defined in the following way:

Assume a plane wave, with intensity I_0 [W m^{-2}], incident on a particle, the total rate of energy removed from this beam to be E [W]. The extinction cross section, σ_t [m^2] is defined as:

$$\sigma_t = \frac{E}{I_o} \tag{2.1}$$

Energy can be removed from this beam by scattering and absorption. The total rate of energy scattered divided by the original intensity gives the scattering cross section (σ_s). The total rate of energy absorbed divided by the intensity gives the absorption cross section (σ_s). From energy conservation it follows that:

$$\sigma_t = \sigma_a + \sigma_s \tag{2.2}$$

The incoming beam transfers momentum to the particle: $E/c = \sigma_t\, I_o/c$. The scattered light emitted by the particle transfers momentum in the forward direction: $\sigma_s\, I_o\, \overline{\cos\theta}/c$. In this way a net pressure cross section (σ_{pr}) can be defined which equals:

$$\sigma_{pr} = \sigma_t - g\, \sigma_s \tag{2.3}$$

Where (the anisotropic factor) $g = \overline{\cos\theta}$ is the average cosine of the scattering angle for a single scattering event.

3

2.3   Optical properties

By describing light transport through tissue with radiative transfer theory, a few assumptions are made. Light is described as a flow of particles, which either scatter elastically or are absorbed by the tissue. This means that phenomena which deal with the wave-like behavior of light (such as interference) are not considered. The optical properties are assumed to be independent of time. (Tissue is characterized by one "average" set of optical properties.) The set of optical properties used are the scattering coefficient μ_s [cm^{-1}], the absorption coefficient μ_a [cm^{-1}], and the angular distribution of the light after being scattered. They are defined below.

If light is travelling in direction $\hat{s}$ over an infinitesimally small distance $d\hat{s}$, the probability that light is being scattered equals $\mu_s \, d\hat{s}$ and the probability that light is being absorbed equals $\mu_a \, d\hat{s}$. The total attenuation coefficient is the sum of the absorption and scattering coefficients:

$$\mu_t = \mu_s + \mu_a \tag{2.4}$$

These bulk optical properties relate to the cross sections given in section 2.2 in the following way. If the scattering (and/or absorbing) particles are sufficiently far away from each other, the scattering events are considered independent [1]. In such a case the scattering (absorption) coefficient equals the scattering (absorption) cross section times the concentration of particles ρ [m^{-3}]

$$\mu_s = \sigma_s \, \rho \tag{2.5}$$

$$\mu_a = \sigma_a \, \rho \tag{2.6}$$

The phase function $p(\hat{s},\hat{s}')$ [sr^{-1}] gives the probability of light, originally traveling in direction $\hat{s}'$, is being scattered in direction $\hat{s}$. The phase function is often rotational symmetric around the original direction. Thus it can be written as a function of the angle θ, or even the cosine of θ, between the original direction and the final direction of propagation: $\hat{s}\cdot\hat{s}' = \cos\theta$. Very often the phase function is written as a sum of Legendre polynomials ($P_n(\cos\theta)$).

---

[1] Van de Hulst [11] considered a distance between the particles of three times the radius sufficient.

4

$$p(\cos\theta) = \sum_{n=0}^{\infty} g_n \frac{2n+1}{2} P_n(\cos\theta) \qquad (2.7)$$

Where g_n is a constant called "the moment of order n". The factor $\frac{2n+1}{2}$ is used for normalization:

$$\int_{-1}^{+1} P_n(\cos\theta) P_m(\cos\theta) \, d(\cos\theta) = \frac{2\,\delta_{nm}}{2n+1} \qquad (2.8)$$

Defined as above (as a probability function) its zero order moment equals 1: (Because a probability function is normalized)

$$\int_{-1}^{+1} p(\cos\theta) \, d(\cos\theta) = 1 = \sum_{n=0}^{\infty} \int_{-1}^{+1} g_n \frac{2n+1}{2} P_n(\cos\theta) \, d(\cos\theta) = g_0 \qquad (2.9)$$

In which $P_0(\cos\theta) = 1$ and equation (2.8) are used.
The first order moment of the phase function is called the anisotropy g: (See also section 2.2.)

$$g = \int_{-1}^{+1} P_1(\cos\theta) \, p(\cos\theta) \, d(\cos\theta) = g_1 = \overline{\cos\theta} \qquad (2.10)$$

The anisotropy is a measure of the fraction of light scattered in the forward direction. ($g = -1$ ⇒ the direction of propagation is turned around, $g = 1$ ⇒ the direction of propagation is left unchanged.)

Usually the Henyey Greenstein phase function ($P_{H.G.}$) is used:

$$P_{H.G.}(\cos\theta) = \frac{1 - g^2}{2\left(1 - 2g\cos\theta + g^2\right)^{3/2}} \qquad (2.11)$$

which is easily mathematically manipulated because all the moments are known: the nth moment equals g^n (= the n-th power of g).

The equation of radiative transfer describes the change of radiance $L(r,\hat{s},t)$ [W m^{-2} sr^{-1}].

At a point r of a surface, in a given direction $\hat{s}$, at time t, the radiance is defined as the radiant intensity of an element of the surface, divided by the area of the orthogonal projection of this element on a plane perpendicular to the given direction. [25] Figure 2.1 illustrates the definition of the radiance. (From Star *et al.* [25])
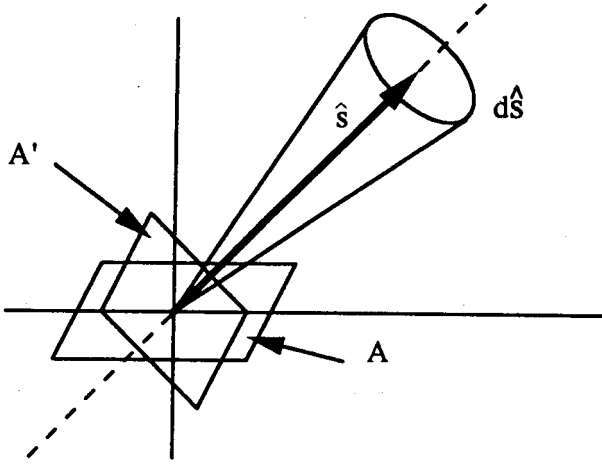
Figure 2.1 At a point r of a surface, in a given direction $\hat{s}$, at time t, the radiance is defined as the radiant intensity of an element of the surface A, divided by the orthogonal projection of this element on a plane perpendicular to the given direction A.

The change of radiance is a sum of losses (due to scattering and absorption) and gains (due to scattering from all other directions into direction $\hat{s}$). This change of radiance is given by the equation of radiative transfer [7] (or the linearized Boltzmann particle transport equation):

$$\frac{1}{c}\frac{dL(r,\hat{s},t)}{dt} = \frac{1}{c}\frac{\partial L(r,\hat{s},t)}{\partial t} + \hat{s}\cdot\nabla L(r,\hat{s},t) =$$

$$-\mu_t\, L(r,\hat{s},t) + \mu_s \int_{4\pi} L(r,\hat{s}',t)\, p(\hat{s}\cdot\hat{s}')\, d\hat{s}' \qquad (2.12)$$

Where

c = the velocity of light in the medium [m s^{-1}].

The important feature of this equation is the second term on the right hand side, which is the contribution of light scattered from all other directions into

direction $\hat{s}$. So, to calculate the radiance at a point at a time in direction $\hat{s}$, the radiance at that point at that time in all other directions has to be known.

Figure 2.2 Scattering and absorption that are considered in the equation of radiative transfer.

2.5   Monte Carlo simulations

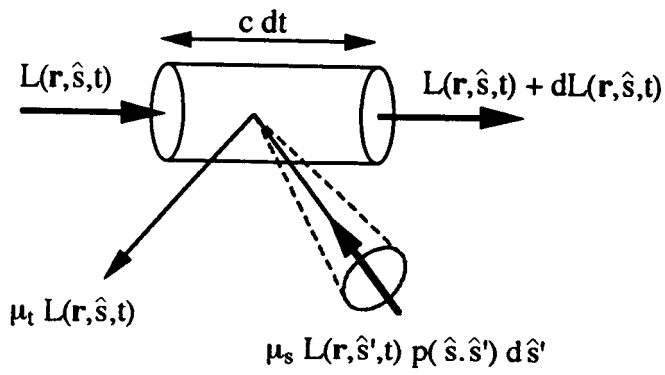Monte Carlo methods simulate the propagation of photons through a tissue. This is done by tracing independent photon paths. These photon paths are determined by several laws of photon propagation. Such a law gives the distribution of a physical quantity (for instance the distance between two scattering events = the step size).

To simulate photon paths, these laws have to be converted into sampling functions. Such a function has a random number ξ ($\in$ (0,1)) as input and a physical (statistical) parameter as output.

The conversion, from a physical law to a sampling function, is considered first (in section 2.5.1) and followed by the different laws of photon propagation with the derived sampling functions (section 2.5.2). Finally (in section 2.5.3) a general set-up for a Monte Carlo simulation program is given.

2.5.1   Sampling functions

A sampling function has a random number ($\xi \in$ (0,1) generated by a random number generator) as input and a physical property as output. The physical property is described by a probability function. For instance Beer's law, that gives the probability ($P_B(z)$ dz) for a photon propagating in the positive z-direction, to have an interaction (either scattered or absorbed) between z and z + dz, can be converted into a probability function:

$$P_B(z) \; dz = \left(\mu_a + \mu_s\right) \exp\left[- \left(\mu_a + \mu_s\right) z\right] dz \qquad (2.13)$$

The factor $(\mu_a + \mu_s)$ in front is used to make it a normalized probability function:

$$\int_{z=0}^{\infty} P_B(z) \; dz = 1 \qquad (2.14)$$
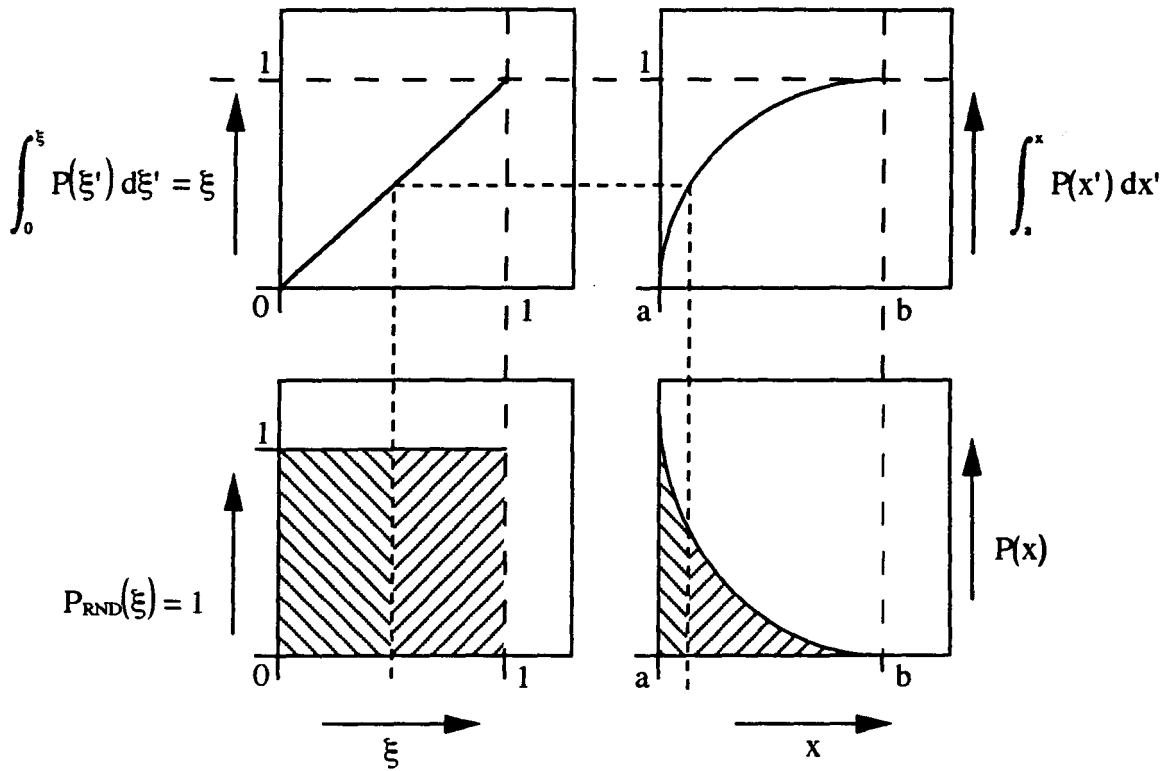
Figure 2.3. Illustration of the construction of a sampling function. Equal surfaces are equally marked. Upper: probability density functions; lower: probability functions; left: a uniform distribution; right: a law of photon propagation. (From Jacques [14])

The probability for an interaction between $z = 0$ and $z = l$ (l = the step size) is given by:

$$\int_{z'=0}^{1} P_B(z') \, dz' = 1 - \exp\left[- \left(\mu_a + \mu_s \right) z \right]$$ (2.15)

and is called the probability density function. This probability density function is in all cases a non-descending function from 0 to 1.

The second probability function used is $P_{RNG}(\xi) = 1$ with the probability density function:

$$\int_{\xi=0}^{\xi} P_{RNG}(\xi') \, d\xi' = \xi$$ (2.16)

This is the uniform probability function generated by the Random Number Generator of the computer. Both probability density functions (2.15) and (2.16) have the same distribution between 0 and 1, thus the step size l can be calculated:

$$l = \frac{-1}{\mu_a + \mu_s} \ln\left[1-\xi\right]$$

(2.17)

The general procedure is given in figure 2.3, in which the different probability and probability density functions are plotted.

2.5.2 Laws of propagation and sampling functions

Beer's law

This has been given in section 2.5.2.

Proportional distributions

A proportional distribution implies, a probability function which is either 1 or 0. The output of a sampling function is one out of two possibilities.
For instance, after determination of the step-size, the probability for a photon to be scattered equals:

$$\frac{\mu_s}{\mu_a + \mu_s}$$

(2.18)

This fraction is called the albedo (a). The probability that a photon is absorbed equals 1 - a. If a random number (ξ not correlated with ξ in equation 2.17) is smaller than the albedo, the photon is scattered, otherwise the photon is absorbed.

A similar distribution is used at boundaries. At a boundary between two layers, with different indices of refraction, the laws of Fresnel [11] are used to determine the probability that a photon is being reflected:

$$R(\theta_i,\theta_t) = \frac{1}{2}\left[\frac{n_i \cos\theta_i - n_t \cos\theta_t}{n_i \cos\theta_i + n_t \cos\theta_t}\right]^2 + \frac{1}{2}\left[\frac{n_t \cos\theta_i - n_i \cos\theta_t}{n_t \cos\theta_i + n_i \cos\theta_t}\right]^2$$

(2.19)

where θ_i is the angle of incidence relative to the normal, n_i is the index of

refraction of the incident medium and θ_t and n_t are the symbols for the transmitted medium. If a random number is smaller than $R(\theta_i, \theta_t)$, then the photon is reflected, otherwise it is transmitted. The cosine notation is used, because the direction of propagation during a simulation, is characterized by the cosines with the Cartesian axes. (See figure 2.4)
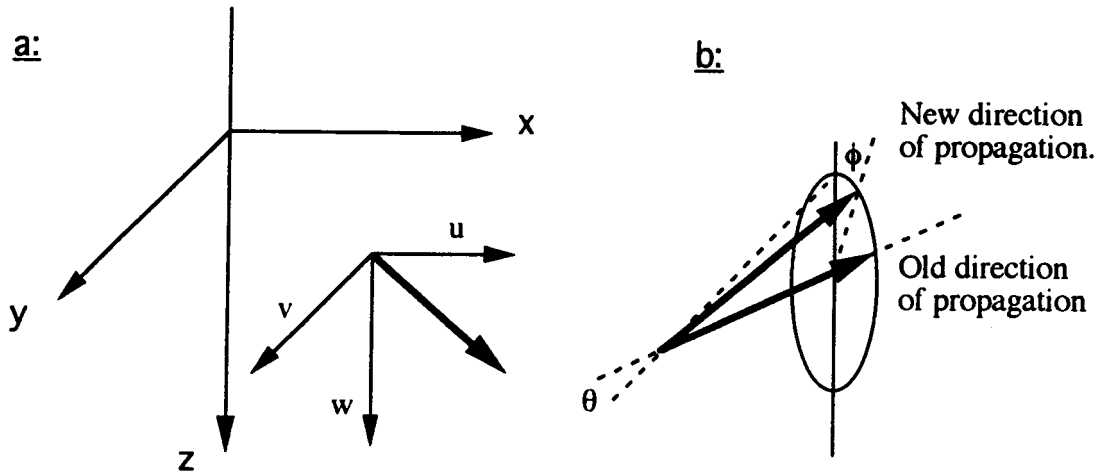
Figure 2.4. Monte Carlo coordinate system. (Adapted from Prahl[23])

a: The Cartesian coordinate system, specification of photon's direction.

b: How θ and ϕ are specified when a photon is scattered.

The phase function:

The phase function gives the probability for a photon, after scattering, to be scattered within the solid angle $d\phi \sin \theta \, d\theta$, with the incident direction. The Henyey Greenstein phase function is used. (See equation (2.11), which is already integrated over the azimuth angle.)

$$P_{H.G.}(\phi,\theta) \, d\phi \, \sin \theta \, d\theta = \frac{1}{4 \pi} \, \frac{1 - g^2}{\left[1 + g^2 - 2 \, g \, \cos \theta\right]^{3/2}} \, d\phi \, \sin \theta \, d\theta \qquad (2.20)$$

Other phase-functions can also be used, but the Henyey Greenstein phase function is used because it is easily mathematically manipulated. Like all probability functions it is normalized

11

$$\int_0^{2\pi} d\phi \int_0^{\pi} P_{H.G.}(\phi,\theta)\ \sin\theta\ d\theta = 1 \tag{2.21}$$

and as with all phase functions the anisotropic factor g is defined as:

$$g = \int_0^{2\pi} d\phi \int_0^{\pi} P_{H.G.}(\phi,\theta)\ \cos\theta\ \sin\theta\ d\theta \tag{2.22}$$

The scattering is assumed independent of the azimuth angle ϕ, this means that the sampling of the angles can be performed independent of each other. The resulting sampling functions are[2]:

$$\phi = 2\ \pi\ \xi \tag{2.23}$$

$$\cos\theta = \frac{1}{2\ g}\left\{1 + g^2 - \left[\frac{1 - g^2}{1 + g - 2\ g\ \xi}\right]^2\right\} \tag{2.24}$$

Equation (2.23) can be found by use of the procedure described in section 2.5.1 and is a solution of:

$$\int_0^{2\pi} d\phi \int_0^{\cos\theta} P_{H.G.}(\phi,\theta)\ \sin\theta\ d\theta = \xi \tag{2.25}$$

The direction of propagation is given by (u, v, w) in which each element represents the cosine of the angle with one of the axis. The new direction of propagation (u^{new}, v^{new}, w^{new}) will be [3]:

---

[2] If the scattering is isotropic, (which means g = 0) then equation 2.23 cannot be used. But in such a case the scattering is also independent of θ so:
$$\cos\theta = 1 - 2\ \xi$$
[3] When w is close to 1 these equations loose accuracy. In that case the following equations should be used:
$$u^{new} = \sin\theta\ \cos\phi$$
$$v^{new} = \sin\theta\ \sin\phi$$
$$w^{new} = \cos\theta$$

$$u^{new} = \frac{\sin\theta}{\sqrt{1 - w^2}} \left(u\ w\ \cos\phi - v\ \sin\phi \right) + u\ \cos\theta \tag{2.26}$$

$$v^{new} = \frac{\sin\theta}{\sqrt{1 - w^2}} \left(v\ w\ \cos\phi + u\ \sin\phi \right) + v\ \cos\theta \tag{2.27}$$

$$w^{new} = -\sin\theta\ \cos\phi\ \sqrt{1 - w^2} + w\ \cos\theta \tag{2.28}$$

Figure 2.4 shows the construction of the new direction.

2.5.3 The program

A photon is characterized by its position (x, y, z) and its direction (u, v, w). The position is in Cartesian coordinates and the direction is given by the cosines with the Cartesian axes. This is done for an easy calculation of new position of a photon after calculating the step size (l):

$$x^{new} = x + u\ l; \qquad y^{new} = y + v\ l; \qquad z^{new} = z + w\ l; \tag{2.29}$$

So all the laws of photon propagation should be given within these parameters: (x, y, z) and (u, v, w).

Snell's law:

One law not yet given is Snell's law which deals with the direction in which a photon is transmitted at boundaries.

$$n_i\ \sin\theta_i = n_t\ \sin\theta_t \tag{2.30}$$

This equation can be rewritten in the desired parameters. With the use of some goniometry this equation becomes:

$$\cos\theta_t = \sqrt{1 - \left(\frac{n_i}{n_t}\right)^2 \left(1 - \cos^2\theta_i\right)} \tag{2.31}$$

So if a photon is transmitted into the next medium, then $\cos\theta$ is calculated and a

new direction is calculated taking into account the normalization of the direction:

$$u^2 + v^2 + w^2 = 1 \qquad (2.32)$$

If a photon is transmitted into the next medium the step size has also to be adapted. Assume that Δl is the remaining step size after the photon has reached the border. The new remaining step size (after crossing the border) will be:

$$\Delta l^{new} = \frac{\left(\mu_a + \mu_s\right)^{old}}{\left(\mu_a + \mu_s\right)^{new}} \Delta l^{old} \qquad (2.33)$$

where equation (2.17) has been used.

Weighting:

An additional parameter, the weight W [J], is given to a photon. This is done to obtain more information out of one simulation. The weight represents an amount of energy. The weight is reduced whenever the program is confronted with a proportional distribution (e.g. a scattering or absorption event) in which case the weight is split. The original weight is one (W = 1).

Splitting:

The weight is split after one step, one fraction of the weight is absorbed, (absorbed = W (1 - a)) and the other fraction becomes the new weight (W → a W). The absorbed part can be registered to give a energy distribution.

The weight is also split if a photon reaches the first or last boundary. One part is reflected and reenters the sample (= R W). The other part is transmitted and registered (W (1 - R)).

Survival roulette:

If the weight is smaller than a *critical weight*, then it has to be terminated, because small weights reveal little information. This is done in such a way that the Law of energy conservation is not violated. A technique called "roulette" is used in which a photon is given a change of 1 over N to survive the roulette. If the photon survives ($\xi < 1/N$), then its weight is multiplied by a factor of N. If the photon dies, then a new photon can be launched.

Flow chart:

A flow chart of a program is given in figure 2.5. The formulas given in the foregoing paragraphs are indicated in this flow graph. For the registration of the reflected and transmitted photons various techniques are used (See section 4.3).

Figure 2.5. Flow chart of a Monte Carlo program. The path most used is printed in bold. In this flow chart the formulas used are printed between brackets.
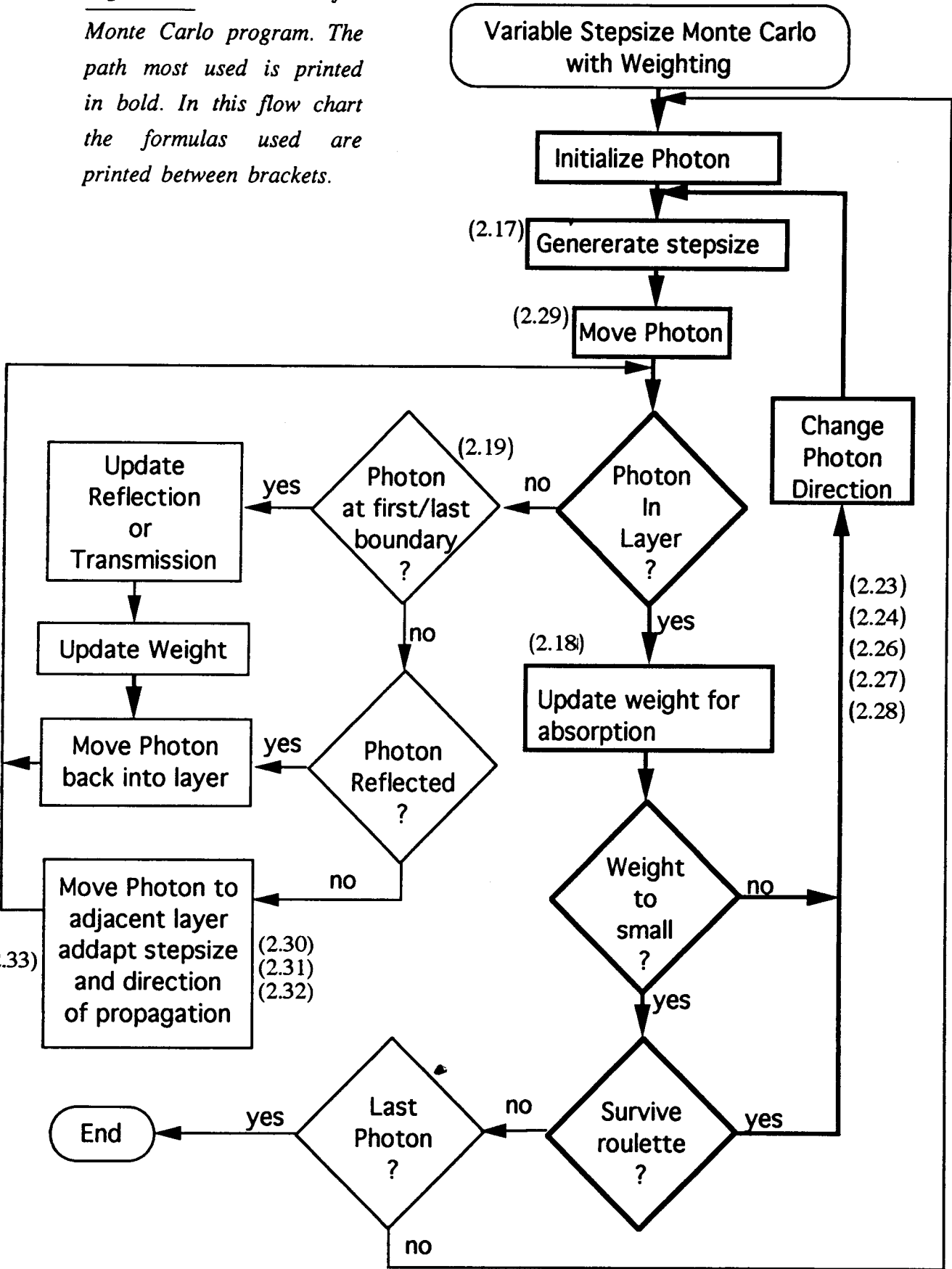
2.6 Adding Doubling

One of the methods to solve the radiative transfer equation, is the Adding Doubling method. The method is based on the fact that once the transmission and reflection for a thin slab are known, the reflection and transmission for a slab of arbitrary thickness may be found by repeatedly doubling the thickness of the thin slab until the thickness desired is reached (This has been called the "interaction principle" [30]).

The advantages of the Adding Doubling method are: it is fast and accurate, one can implement any phase function desired, Fresnel boundary conditions can be implemented and inhomogeneous layer properties can be added.

The Adding Doubling method is a solution of the radiative transfer equation in case of steady state and a slab geometry in which the optical properties are either constant or a function of depth (z) only. Only the azimuthally averaged intensity (i(z) in [W]) is considered:

$$i(z, \cos\theta) = \int_{-\infty}^{\infty} dx \int_{-\infty}^{\infty} dy \int_{0}^{2\pi} d\phi \ L(x,y,z,\phi,\cos\theta) \tag{2.34}$$

This averaged intensity is made discrete for various angles.

$$i(z) = \begin{pmatrix} i(z, \pm\cos\theta_1) \\ i(z, \pm\cos\theta_2) \\ \vdots \\ i(z, \pm\cos\theta_n) \end{pmatrix} \tag{2.35}$$

The number of angles is always even; when only two angles are used the method is called the Delta Eddington method. The number of angles is referred to as the number of fluxes used.

The azimuthally averaged radiative transfer equation satisfies [30]:

$$\cos\theta \ \frac{\partial i}{\partial z} + \mu_t \ i = \mu_s \int_{-1}^{1} \overline{P(\cos\theta, \cos\theta')} \ i(z, \cos\theta') \ d\cos\theta' \tag{2.36}$$

where $\overline{P(\cos\theta, \cos\theta')}$ is the azimuthally averaged phase function.

17

Due to the discretization, the integration can be replaced by a summation. The equation can be split into two equations by separating all the positive and all the negative fluxes. Finally all the equations can be integrated over a small distance $\Delta\tau$ (With an appropriate integration formula) and the reflected and transmitted intensities for a sample of thickness $\Delta\tau$ are obtained, where τ is the optical thickness:

$$\tau = \mu_t \, d \tag{2.37}$$

where d [cm] is the physical thickness.

The reflected and transmitted intensities, of a sample of thickness τ can be found by doubling the thickness until the (optical) thickness desired is achieved. If needed two glass slides can be added, using the Law's of Fresnel. The total intensity reflected can be found by integrating over the contributions of all angles.

2.7   Time of flight measurements

Time of flight measurements are mainly performed to investigate the possibilities for imaging applications. The general idea is that the time of flight of a photon through tissue tells something about the distance travelled by the photon (= the optical path). The intensity, after a certain time of flight, reveals information about the interaction of the photons with the tissue, over that distance.

The time resolved measurements described in this report are for the determination of optical properties. The theory which currently describes these kind of experiments best, is the diffusion theory. The diffusion equation can be derived as an approximation of the radiative transfer equation. For the derivation of the diffusion equation, it is assumed that that the influence of boundaries is negligible and the absorption coefficient is much smaller than the scattering coefficient. In that case the diffusion equation for the fluence rate can be derived.

2.7.1   Diffusion theory

The diffusion theory is used to calculate the (radiant energy) fluence rate $\phi(r,t)$. The fluence rate [W m^{-2}] is defined as: "at a given point in space, the radiant energy flux incident on a small sphere, divided by the cross-sectional area of that sphere" (ISO 31/6, 1980) The fluence rate is related to the radiance by

$$\phi(r,t) = \int_{4\pi} L(r,\hat{s},t) \, d\hat{s} \tag{2.38}$$

The diffusion equation is given by:

$$\left[\gamma^2 \, \nabla^2 - \mu_a \, c - \frac{\partial}{\partial t}\right] \phi(r,t) = -q(r,t) \tag{2.39}$$

where

$$\gamma^2 = \frac{c}{3\left[\mu_a + \mu_s(1 - g)\right]} = \text{the diffusion coefficient [m}^2 \text{ s}^{-1}] \tag{2.40}$$

and

$q(r,t) = $ a source function [W m^{-2} s^{-1}].

19

The diffusion equation can be derived from the radiative transfer equation by considering the first two moments of the radiance $L(r,\hat{s},t)$ [25].

The diffusion equation has to be solved in a volume Ω bounded by a surface $\partial\Omega$. In particular the output flux, $\Gamma(\zeta,t)$ [W s^{-1} m^{-2}], is calculated

$$\Gamma(\zeta,t) = -\gamma^2 \frac{\partial}{\partial\hat{n}}\phi(r,t)\bigg|_{\partial\Omega} = -\gamma^2\,\hat{n}\cdot\nabla\phi(r,t)\bigg|_{\partial\Omega} \qquad (2.41)$$

where:

ζ = a point on $\partial\Omega$

$\hat{n}$ = the outward surface normal.

This time dependent flux expression corresponds to the measurement of intensity as a function of time.

3. Integrating sphere theory

3.1 Introduction

Integrating spheres are used to determine the reflectance and transmittance of a sample. In this chapter the power detected in a sphere is derived from signal flow graphs and related to the sphere geometry and reflection and transmission factors of the sample. Signal flow graphs are originally used in feedback theory of electrical networks [15], but are also used in process control theory [9]. It will be shown below that the light distribution within an integrating sphere can also be described by these graphs.

The integrating sphere theory is based on the work by J.W. Pickering *et al.* and an extensive treatment can be found in his work [19] [20]. This theory is improved, in this report, by distinguishing between light originating from the sample and light originating from the inner sphere wall. The former cannot be incident on the sample again, as was assumed by Pickering *et al.*, while the latter can be incident on the sphere wall and on the sample. The reason is that the sample is flat and the sphere wall is curved. Pickering *et al.* did not incorporate this distinction in his theory.

The following subjects are dealt with in this chapter:
- Signal flow graphs, how to construct signal flow graphs and how to use them to derive the transfer from input to output (section 3.2) (From Mason [15]).
- Single sphere formulas, related to either reflection or transmission measurements (section 3.3).
- Double sphere formulas which are used in a double integrating sphere setup (section 3.4).
- The calibration of the integrating spheres (section 3.5).
The nomenclature used is summarized in table I page IV and V.

3.2 Signal Flow Graphs

A signal flow graph is a network of directed branches which connect at nodes. Branch jk originates at node j and terminates upon node k, the direction from j to k being indicated by an arrowhead on the branch. Each branch jk has a parameter associated with it called the branch gain g_{jk} and each node j has an associated parameter

called the node signal x_j. The various node signals x_j are related by the equations

$$\sum_j x_j \, a_{jk} = x_k \tag{3.1}$$

The graph shown in figure 3.1, for example, has equations:

$$a_{12} \, x_1 + a_{32} \, x_3 = x_2$$
$$a_{23} \, x_2 + a_{43} \, x_4 = x_3$$
$$a_{24} \, x_2 + a_{34} \, x_3 = x_4$$
$$a_{35} \, x_3 + a_{45} \, x_4 = x_5 \tag{3.2}$$

The following definitions are used. A *source* is a node having only outgoing branches (node 1 in figure 3.1). A *sink* is a node having only incoming branches (node 5 in figure 3.1). A *path* is any continuous succession of branches traversed in the indicated branch directions. A *forward path* is a path from source to sink along which no node is encountered more than once ($a_{12}a_{23}a_{34}a_{45}$, $a_{12}a_{24}a_{45}$, $a_{12}a_{24}a_{43}a_{35}$, $a_{12}a_{23}a_{35}$, in figure 3.1). A *feedback loop* is a path that forms a closed cycle along which each node is encountered once per cycle. ($a_{23}a_{32}$, $a_{34}a_{43}$, $a_{24}a_{43}a_{32}$, but not $a_{23}a_{34}a_{43}a_{32}$, because node 3 is encountered twice per cycle, in figure 3.1). A *path gain* is the product of the branch gains along that path. The *loop gain* of a feedback loop is the product of the gains of the branches forming that loop. The *gain of a flow graph* is the signal appearing at the sink per unit signal applied at the source. Only one source and one sink need be considered since sources are superimposable and sinks are independent of each other.
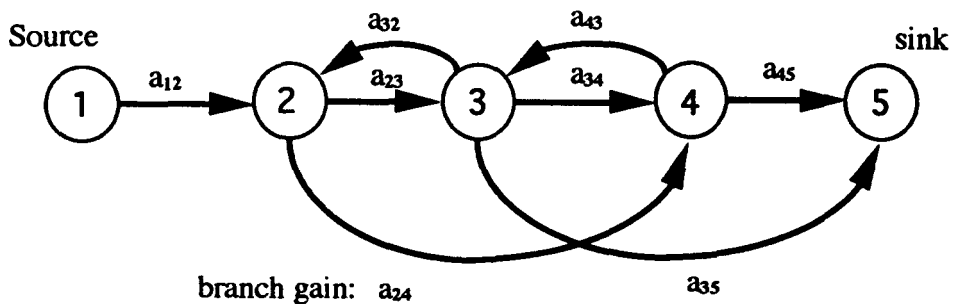

Figure 3.1. a simple signal flow graph.

22

According to Mason [15] the gain of a flow graph is given by

$$G = \frac{\sum_{k} G_k \Delta_k}{\Delta} \tag{3.3}$$

where

G_k = gain of the kth forward path.

Δ = the discriminant

$$\Delta = 1 - \sum_{m} P_{m1} + \sum_{m} P_{m2} - \sum_{m} P_{m3} + \ldots \tag{3.4}$$

P_{mr} = gain product of the mth possible combination of r non touching loops.

Δ_k = The value of Δ for that part of the graph not touching the kth forward path.

The reader is referred to Mason's paper for further explanations. For figure 3.1 the gain of the flow graph is given by:

$$\frac{x_5}{x_1} = \frac{a_{12}a_{23}a_{34}a_{45} + a_{12}a_{24}a_{45} + a_{12}a_{23}a_{35}}{1 - a_{23}a_{32} - a_{34}a_{43} - a_{43}a_{32}a_{24}} \tag{3.5}$$

where

$G_1 = a_{12}a_{23}a_{34}a_{45};$ $G_2 = a_{12}a_{24}a_{45};$ $G_3 = a_{12}a_{23}a_{35};$

$P_{11} = a_{23}a_{32};$ $P_{12} = a_{34}a_{43};$ $P_{13} = a_{43}a_{32}a_{24};$

$\Delta_1 = \Delta_2 = \Delta_3 = 0;$ $\Delta = 1 - a_{23}a_{32} - a_{34}a_{43} - a_{43}a_{32}a_{24}.$

In the integrating sphere theory the source will be the light (with power P) entering the sphere. The sink will be the detector (with detected power P_d). The branches will be determined by the direction in which the light travels. The gain will be the fraction of the light travelling from one part of the sphere to the other part.

3.3 Single spheres

The calculations are performed for a sphere with a detector which does not receive light from the sample. (See figure 3.2). The construction of the sphere is shown in figure 3.3. Each sphere has three ports: one to illuminate the sample, (the *entry* port[4]), one that contains the sample is, (the *sample* port), and one in which the detector is placed, (the *detector* port). The construction of the sphere is here such

---

[4] The sphere can also be used in transmission. In that case the collimated transmitted light leaves the sphere through this aperture, called the *exit* port.

that the collimated (or specular) reflection is leaving the sphere through the entry port. Other configurations can also be handled and will only require slight modifications of the calculations presented below.
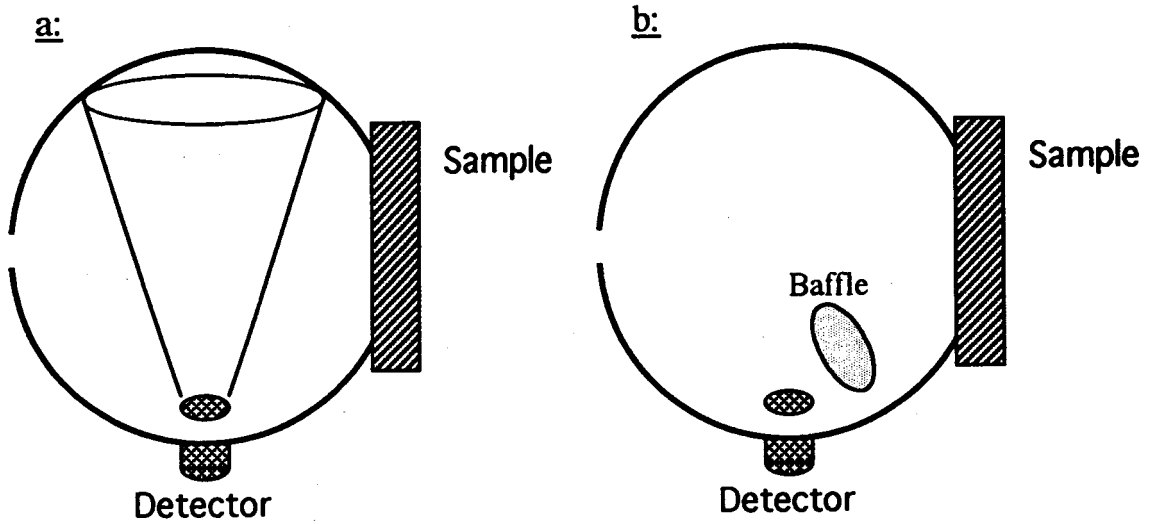
Figure 3.2. Two ways to make the detector not see the sample:

a: A non-isotropic detector.

b: Using a baffle (which has the same diffuse coating as the sphere wall).
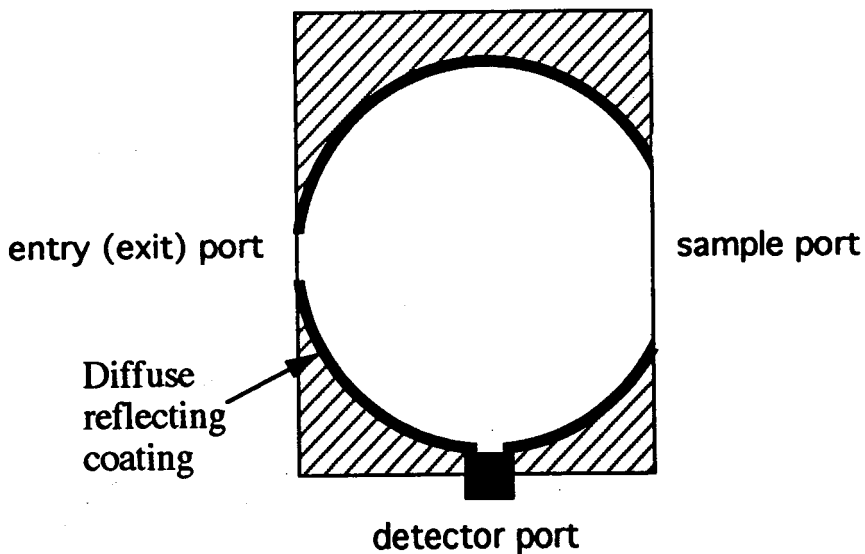
Figure 3.3. Construction of the integrating sphere.

The following setup is assumed (see figure 3.4a): the sample is placed at the sample port of the integrating sphere, the light enters the sphere through the entry port, light hits the sphere wall first and the sample is diffusely irradiated by the sphere wall.

Light which hits the sphere wall will be diffusely reflected by a factor m (usually m is close to one). The reflection is assumed to be completely Lambertian. This means that the intensity reflected is equally distributed over all angles. The power reflected is distributed homogeneously over the different parts of the sphere. (Because of the sphere geometry.)

a: *b:*
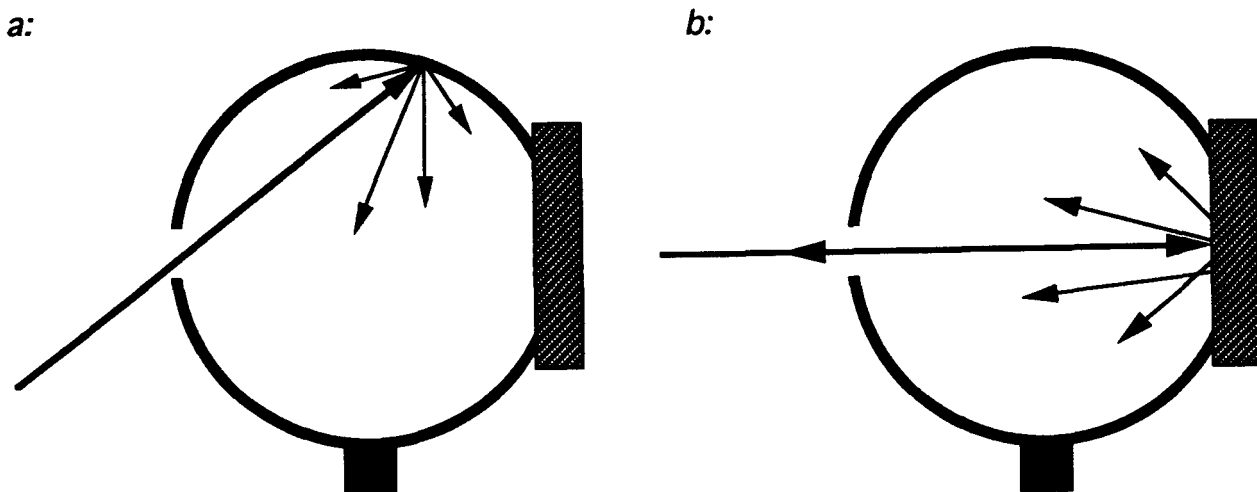
Figure 3.4. Set-up used for reflection measurements:

a: Light is first incident on the sphere wall.

b: Light is first incident on the sample.

Light which propagates from the sphere wall to the sample will have a gain factor of:

$$m \, \frac{s}{A} \tag{3.6a}$$

where s = the sample area [m^2], and A = the total sphere area including all parts. [m^2]

Light which propagates from the sphere wall to the detector will be detected with a

gain factor of:

$$m \, \beta \, \frac{\delta}{A} \qquad (3.6^b)$$

where δ = the detector area [m²], β = the efficiency of the detection which includes that the detector only sees part of the sphere wall.

Light which propagates from the sphere wall to other holes will have a gain factor of:

$$m \, \frac{h}{A} \qquad (3.6^c)$$

where h = the area of holes [m²].

Light which propagates from the wall back to the sphere wall has a gain factor of:

$$m \, \alpha \qquad (3.6^d)$$

where α = the relative total inner surface area of the sphere excluding all other parts of the inner sphere:

$$\alpha = \frac{A - s - h - \delta}{A}$$

For the situations that the detector receives the light first reflected, part of the signal flow graph is given in figure 3.5 . This signal flow graph is not complete. Reflection from all parts of the sphere has to be accounted for. It is assumed that only the sample reflects light with a diffuse reflection factor R_d and that this light reflected is completely Lambertian. The following gain factors will result from it.

Light which travels from the sample to the holes will have a gain factor of:

$$R_d \, \frac{h}{A - s} \qquad (3.6^e)$$
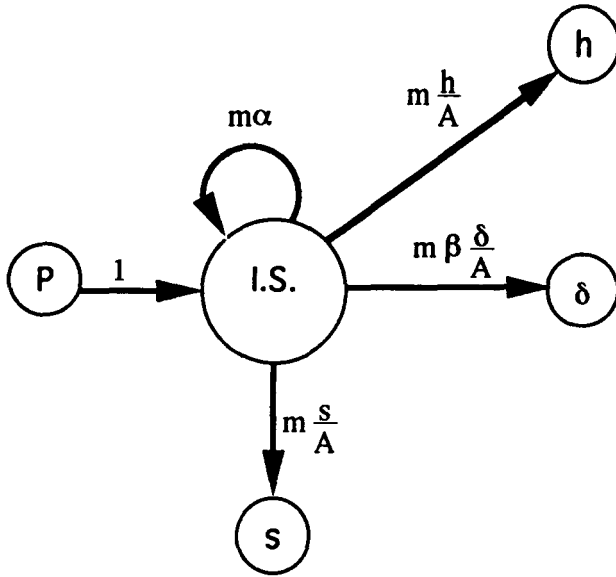
Light which travels from the sample to the sphere wall will have a gain factor of:

$$R_d \left[1 - \frac{h}{A - s} \right] \qquad (3.6^f)$$

The complete signal flow graph is given in figure 3.6a. From this figure and according to Mason (equation 3.3), the power detected is given by

$$\frac{P_d}{P} = \frac{m \, \beta \, \dfrac{\delta}{A}}{1 - m \, \alpha - m \, \dfrac{s}{A} \, R_d \left[1 - \dfrac{h}{A - s} \right]} \qquad (3.7)$$

If collimated light is first incident on the sample (figure 3.4b), then a distinction is made between the first reflection by the sample and all other reflections. This is because the diffuse reflection factor for collimated light (R_{cd}) differs from the diffuse reflection factor for diffuse light (R_d). The signal flow graph for this case is given in figure 3.6b, form which follows:

$$\frac{P_d}{P} = \frac{R_{cd}\left(1 - \frac{h}{A-s}\right) m\, \beta\, \frac{\delta}{A}}{1 - m\,\alpha - m\,\frac{s}{A}\,R_d\left(1 - \frac{h}{A-s}\right)} \qquad (3.8)$$

In this case it is assumed that the collimated reflection (R_c) leaves the sphere trough the entry port.

Figure 3.6. Complete signal flow graphs:
a: Light is first incident on the sphere wall.
b: Light is first incident on the sample.
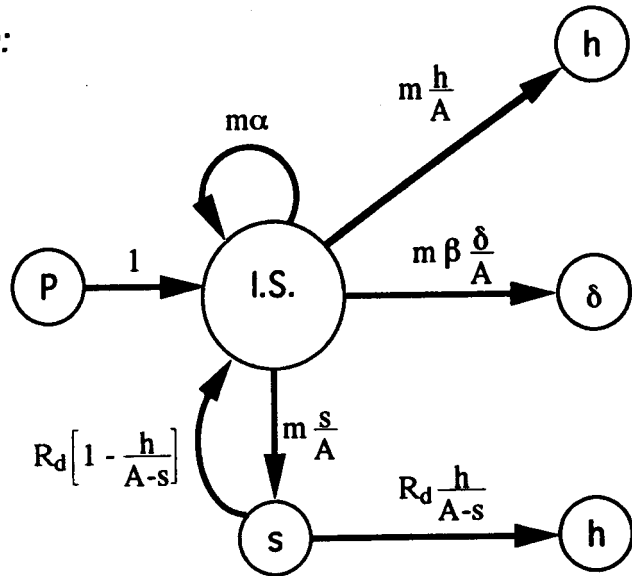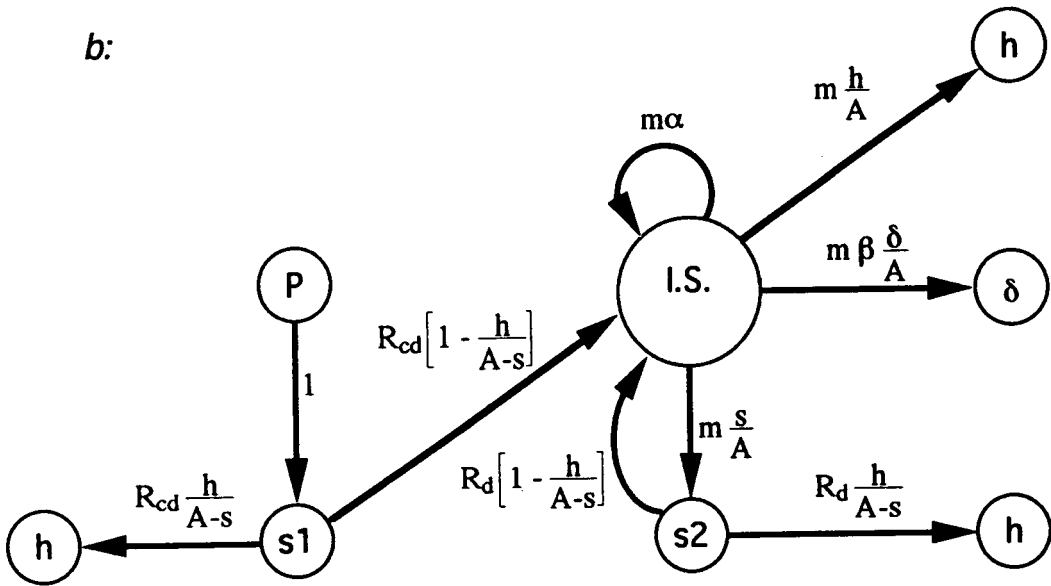
3.3.2 Transmission

The following setup is assumed: (see figure 3.7) The sample is placed at the sample port of the integrating sphere. The light enters the sphere through the sample. The collimated transmission leaves the sphere through the exit port.

With gains similar to those before a similar signal flow graph can be made as before. This is given in figure 3.8. From this signal flow graph we find

$$\frac{P'_d}{P} = \frac{T_{cd}\left[1 - \frac{h'}{A'-s}\right] m' \beta' \frac{\delta'}{A'}}{1 - m'\alpha' - m'\frac{s}{A'}'R_d\left[1 - \frac{h'}{A'-s}\right]} \tag{3.9}$$

Where T_{cd} is the diffuse transmission coefficient for collimated incident light. The prime (') is used to indicate the parameters of the transmission sphere.
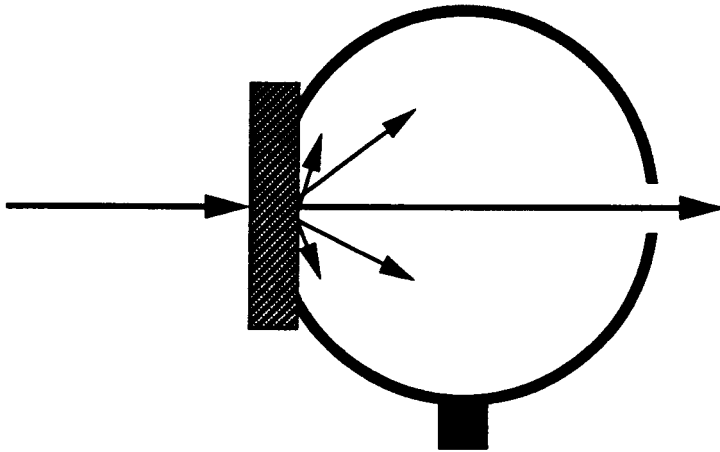
Figure 3.7. Set-up used for the transmission measurement.

Figure 3.8. Signal flow graph for the transmission measurement.
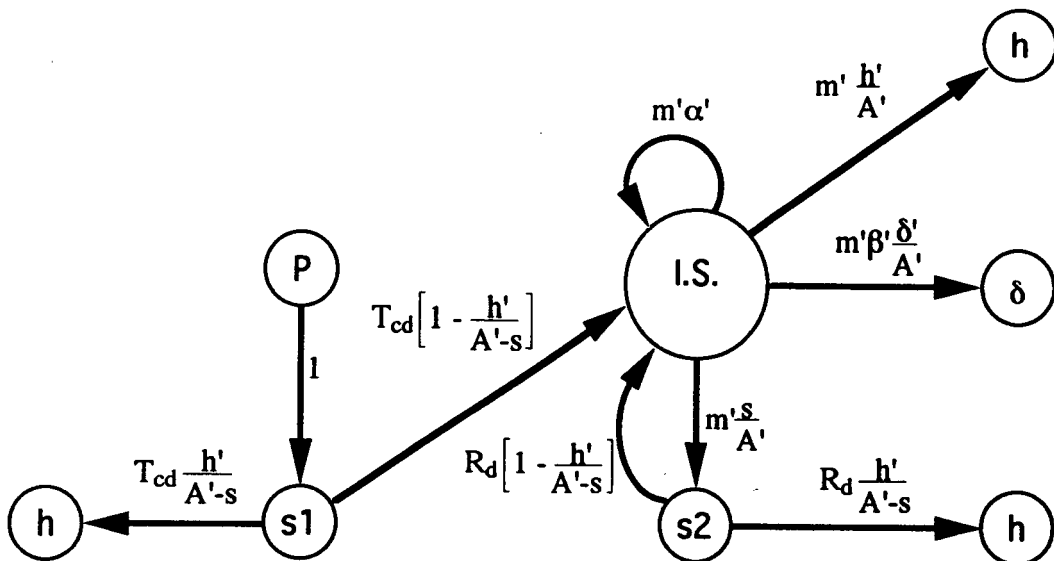
3.4 Double spheres

The double integrating sphere setup is shown in figure 3.9. In this case the sample is placed between the two integrating spheres. The sample can be illuminated by the sphere wall (figure 3.9a), or directly by the beam (figure 3.9b). In the latter case the collimated reflection and collimated transmission are assumed to be leaving the spheres.
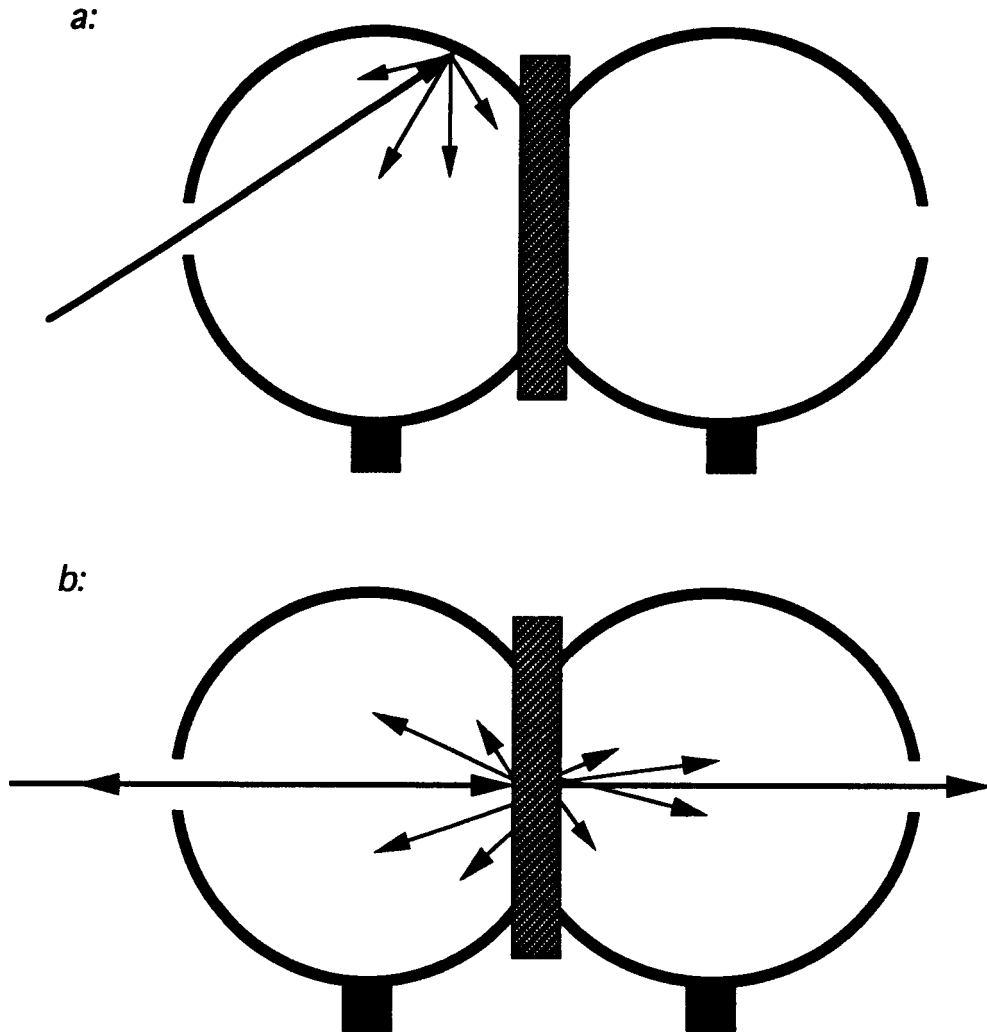
Figure 3.9. The double integrating sphere set-up:

a: Light is first incident on the wall of the reflection sphere.

b: Light is first incident on the sample.

For the derivation of the gain of the flow graphs the following substitutions are made:

$$b_1 = \left[1 - \frac{h}{A - s}\right] m \, \beta \, \frac{\delta}{A} \qquad (3.10)$$

$$b_2 = m \, \frac{s}{A} \left[1 - \frac{h}{A - s}\right] \qquad (3.11)$$

$$b_3 = m \, \alpha \qquad (3.12)$$

From figure 3.10a, for the case that light is first incident on the sphere wall, it follows:

$$\frac{P_d}{P} = \frac{m \, \beta \, \frac{\delta}{A} \left(1 - b_2' R_d - b_3'\right)}{1 - b_3 - b_3' - b_2 R_d - b_2' R_d - b_2 T_d b_2' T_d + b_3 b_2' R_d + b_3' b_2 R_d + b_3 b_3' + b_2 R_d b_2' R_d} \qquad (3.13)$$

$$\frac{P_d'}{P} = \frac{m \, \beta \, \frac{\delta'}{A'} T_d \left(1 - b_2 R_d - b_3\right) m \, \frac{s}{A}}{1 - b_3 - b_3' - b_2 R_d - b_2' R_d - b_2 T_d b_2' T_d + b_3 b_2' R_d + b_3' b_2 R_d + b_3 b_3' + b_2 R_d b_2' R_d} \qquad (3.14)$$

In which primes are used to distinguish between the reflection sphere (without a prime) and the transmission sphere (with a prime). From figure 3.10b, for the case that light is first incident on the sample, it follows:

$$\frac{P_d}{P} = \frac{R_{cd} \, b_1 \left(1 - b_3' - b_2' R_d\right) + T_{cd} \, b_2' T_d b_1}{1 - b_3 - b_3' - b_2 R_d - b_2' R_d - b_2 T_d b_2' T_d + b_3 b_2' R_d + b_3' b_2 R_d + b_3 b_3' + b_2 R_d b_2' R_d} \qquad (3.15)$$

$$\frac{P_d'}{P} = \frac{T_{cd} \, b_1' \left(1 - b_3 - b_2 R_d\right) + R_{cd} \, b_2 T_d b_1'}{1 - b_3 - b_3' - b_2 R_d - b_2' R_d - b_2 T_d b_2' T_d + b_3 b_2' R_d + b_3' b_2 R_d + b_3 b_3' + b_2 R_d b_2' R_d} \qquad (3.16)$$

The above four formulas have the same denominator, which is obvious from the different signal flow graphs. By rearranging different terms, the denominator becomes:

$$\left(1 - b_3 - b_2 R_d\right)\left(1 - b_3' - b_2' R_d\right) - b_2 T_d b_2' T_d \qquad (3.17)$$

a:
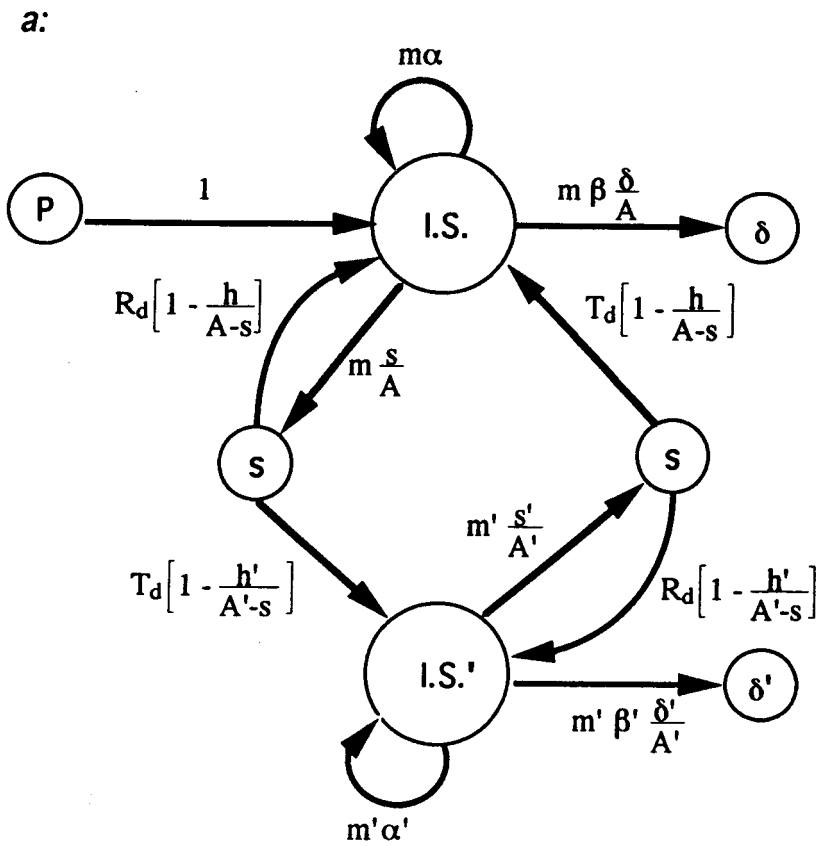
Figure 3.10.

Signal flow graphs for the double integrating sphere set-up. The holes are left out.

a: Light is first incident on the wall of the reflection sphere.

b: Light is first incident on the sample.

b:
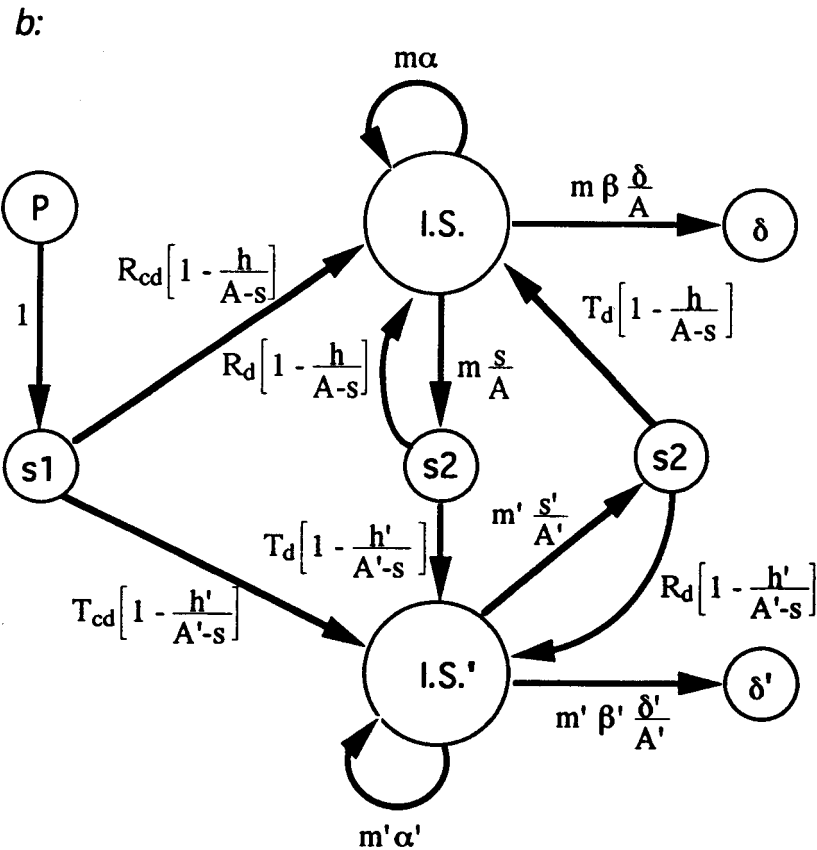
3.5   Calibration

The sphere constants b_1, b_2 and b_3 can be calculated or measured. The measurement of the sphere constants can be done with the use of Reflectance standards. In case light is first incident on the sample the voltage detected satisfies [5]

$$V_\% = \frac{B_1 \, R_{cd}}{1 - B_2 \, R_d} \tag{3.18}$$

where equation 3.10, 3.11 and 3.12 are used with,

$V_\%$ is the voltage (or current) measured by a detector [V] or [A].

$$B_1 = K \frac{b_1}{1 - b_3} = K \frac{\left(1 - \dfrac{h}{A - s}\right) \dfrac{\delta}{A} \, \beta \, m}{1 - m \, \alpha} \tag{3.19}$$

K is a proportional constant [V] (or [A]), which is the efficiency of the detector.

$$B_2 = \frac{b_2}{1 - b_3} = \frac{\left(1 - \dfrac{h}{A - s}\right) \dfrac{s}{A} \, m}{1 - m \, \alpha} \tag{3.20}$$

It is assumed that R_{cd} equals R_d for the reflectance standards. Rewriting equation 3.18 yields:

$$\frac{V_\%}{R_d} = B_1 + B_2 \, V_\% \tag{3.21}$$

One can determine the two sphere constants by plotting $V_\%/R_d$ versus $V_\%$. It is noted that B_2 will be independent of the incident laser power and the reflectance standards used. B_2 will only be determined by the sphere geometry used and the reflectance value of the sphere wall. Thus B_2 needs not to be determined during every measurement. B_2 tells something about how good the "integrating effect" is. See figure 3.11.

[5] b_3 is not of interest with the set-up used. b_3 plays only a role when light is first incident on the sphere wall.

B_1 depends on the incident power. Thus B_1 needs to be determined every time a measurement is performed.

Figure 3.11.
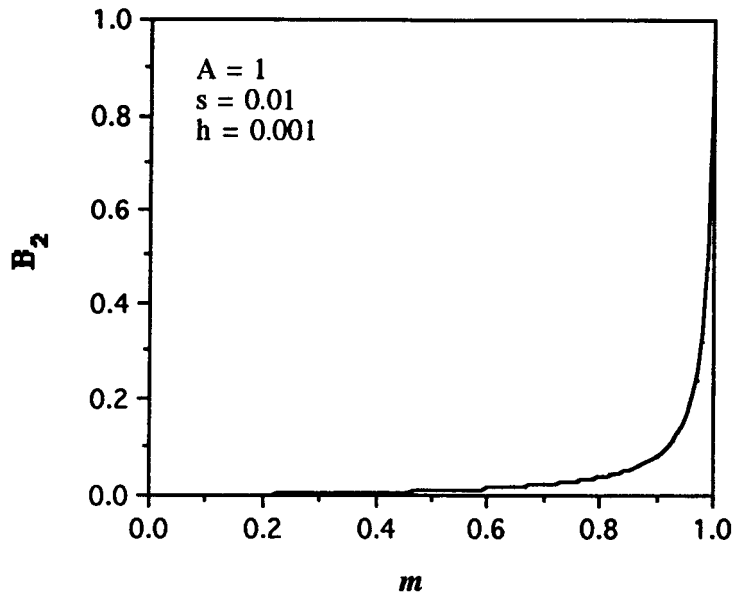
Figure 3.11. The second sphere constant B_2, which determines the integrating effect, as a function of the reflection factor of the sphere wall, m.

4. Materials and methods

4.1 Introduction

To investigate the determination of optical properties with the use of integrating spheres, the following simulations and experiments were performed.

Monte Carlo simulations were performed to investigate the light distribution within integrating spheres (section 4.3). The Monte Carlo program was written by Marleen Keijzer (Delft, The Netherlands) and adapted to calculate the light distributions within an integrating sphere.

Integrating sphere measurements were performed to investigate the dependence of the optical properties of a sample on its thickness (section 4.4). This was done with two phantom materials: Intralipid® and Polystyrene (section 4.2). The sphere formulas (chapter 3) were implemented in an inverse adding doubling program (section 2.6).

Time resolved measurements were performed with the same phantom materials. This was done in order to obtain a second independent measurement of the optical properties (section 4.5). This was done with a set-up used for time resolved transillumination imaging [12].

4.2 Materials

In this study two phantom materials were used: Intralipid-10% (Kabivitrum, Stockholm, Sweden) and polystyrene (Polysciences Inc., St. Goar, Germany). These materials were used because they are (similar to tissue) having a high scattering coefficient and a high anisotropic factor (for skin $\mu_s \simeq 500$ cm^{-1} and g $\simeq$ 0.8 [2]). Intralipid was diluted with 9% NaCl until 0.5%, 1.0%, 1.5% and 2.0% concentrations[6]. Polystyrene was diluted with distilled water until 0.05%, 0.10%, 0.167%, 0.227%, 0.417% and 0.714% concentrations. Both phantoms were available from another study [12]. No absorbers were added.

Polystyrene consists of latex spheres ⌀ = 0.99 μm ± 0.004 μm in water. Mie calculations (section 2.2) were performed. Results of these calculations are given in table 4.1.

---

[6] 1.0 % dilution means 1 part Intralipid-10% and 9 parts 9% NaCl.

	$\lambda = 633$ nm.	$\lambda = 780$ nm.
σ_s/A	2.6998	2.0051
σ_a/A	0.0000	0.0000
σ_{pr}/A	0.2321	0.2078
g	0.9140	0.8964

Table 4.1. The results of Mie calculations:

The input parameters were:
- *index of refraction n: 1.6 (latex); 1.33 (water)*
- *wavelength (in vacuum): 632.8 nm and 780 nm.*
- *diameters spheres: 990 nm.*
No absorption was added.
A is the physical cross section of the particle.

4.3   Monte Carlo simulations

The program used follows independent photon paths in a five layer structure. (Air, glass, tissue, glass, air) These structures are plane parallel and the z-axis was chosen perpendicular to the layer interfaces. (See figure 4.1) The photons were launched at the air glass boundary and were registered as they left the glass air boundary (on either side).

The input for a simulation consists of:

- optical properties (μ_a, μ_s, g) of the turbid medium,
- the indices of refraction of the turbid medium and of the glass,
- the dimensions of the sample and of the integrating spheres.

The output of a simulation is a distribution of light coming from the sample.
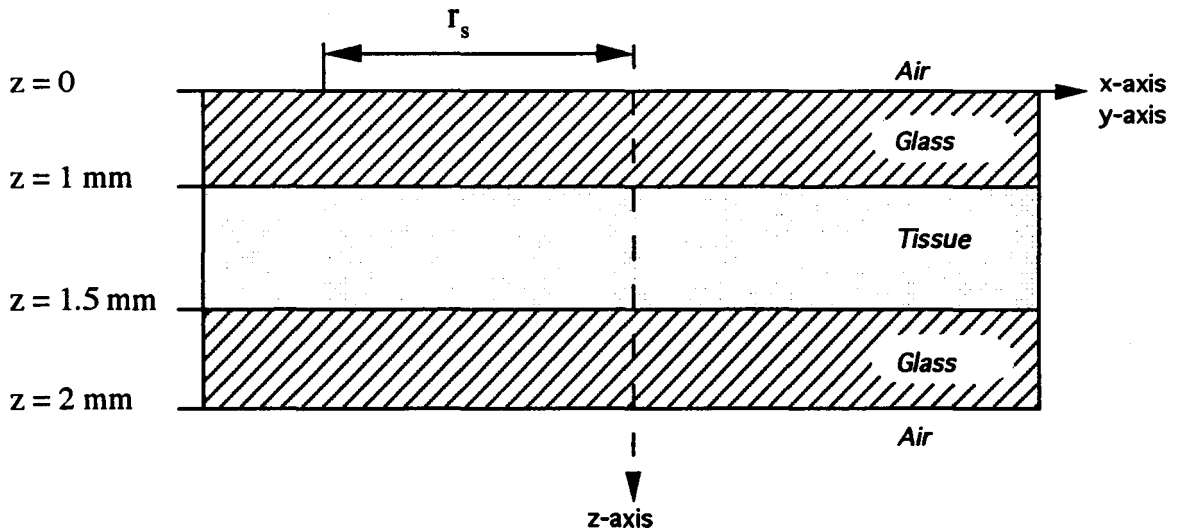
Figure 4.1. The five layer structure used in the simulations.

Photons enter the spheres when they leave the glass air boundary within distance r_s (The radius of the sample port.)
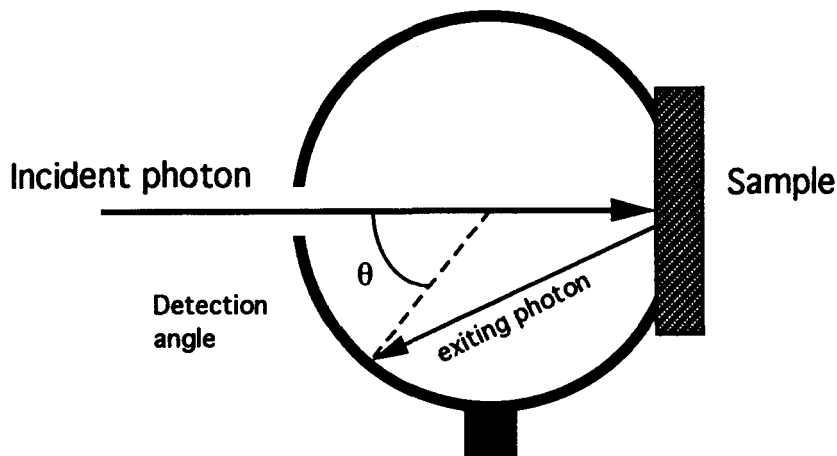
Figure 4.2.

Illustration of the detection angle within an integrating sphere.

Two series of simulations were performed. In the first series all photons were launched at the center of the sample perpendicular to the surface. This was done to simulate the illumination with a laser beam. The output of these simulations is a reflection and transmission coefficient for collimated irradiation (R_{cd} and T_{cd}). The photons were detected as a function of the angle θ within a sphere (see figure 4.2). Table 4.2 gives the input for the first series of simulations.

Table 4.2. The input parameters used for the first series of simulations. τ ranged from 2 to 16. The albedo was kept constant (a = 0.99) 50.000 photons were launched. The critical weight equaled 0.0001.

Layer	Index of refraction	μ_a [cm^{-1}]	μ_s [cm^{-1}]	g	thickness [μm]
air	1				
glass	1.55	0.00001	0.00001	0	1000
tissue	1.37	0.2*τ	19.8*τ	0.8	500
glass	1.55	0.00001	0.00001	0	1000
air	1				

In the second series diffuse illumination of the sample was simulated, to investigate the illumination of the sample by the sphere. This was done in three steps.

The first step was a Monte Carlo simulation. All the photons were launched Lambertian" at r = 0 for discrete angles:

$$\cos \theta_i = 1 - \frac{1}{n + 1} * i \qquad i = 1, 2, \ldots, n \qquad (4.1)$$

38

Figure 4.3. Illustration of a convolution with a circular beam profile. The radius of the illuminating beam is r_s. (From Prahl [23])
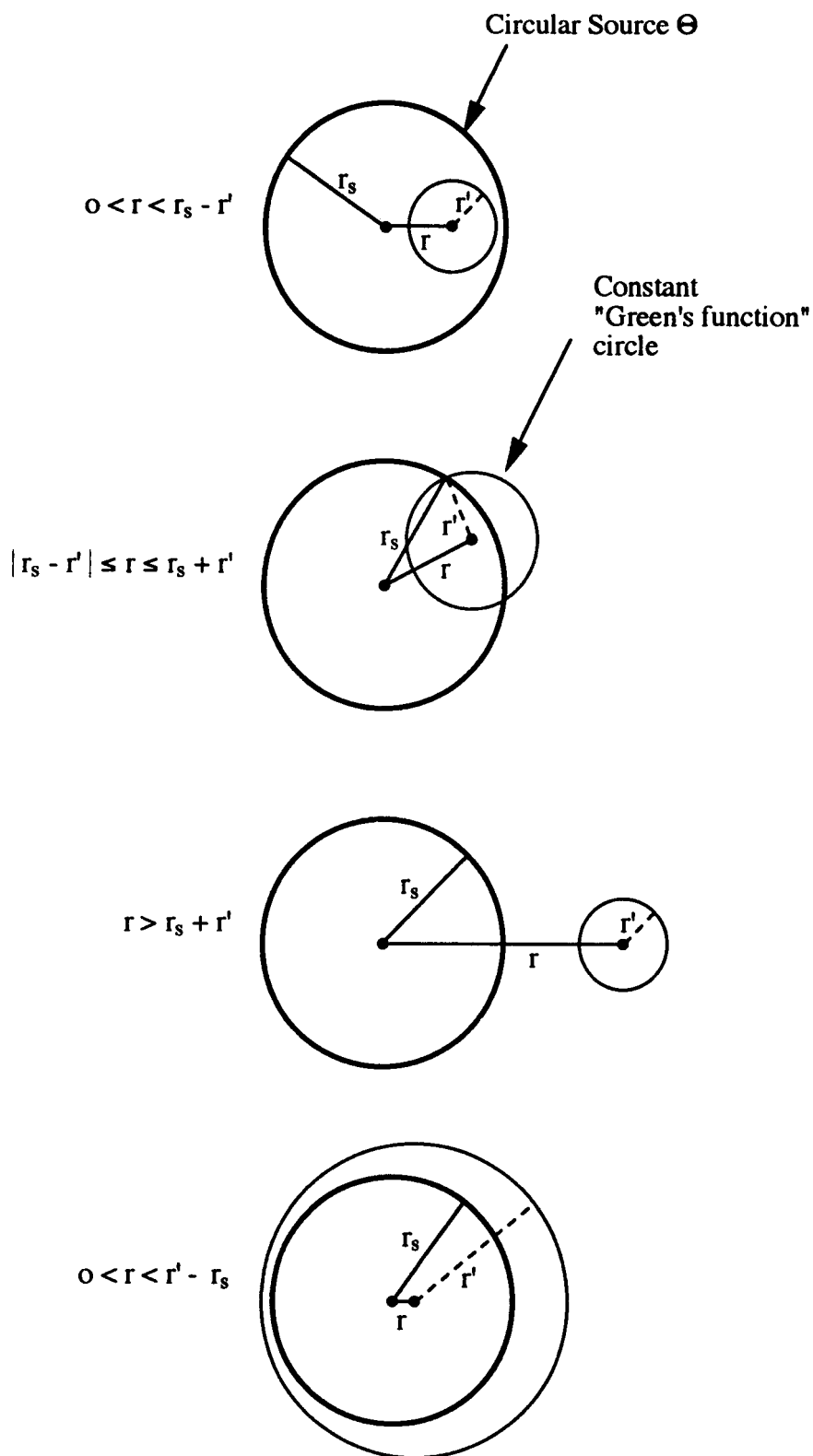
The weights of the exiting photons were registered as a function of the lateral distance travelled R(r) and T(r). (R(r) and T(r) can be seen as Green's functions.)

The second step was the calculation of the reflected Φ(r) and transmitted light intensities if the sample was illuminated homogeneously by a circular source. This was done by convolving the reflection profile R(r) (and transmission profile T(r)) with a circular source (Θ), with a uniform light distribution ranging from zero to the radius of the sample port, r_s. See figure 4.3 (From Prahl [23]).

$$\Phi(r) = \int_0^\infty R(r') \; \Theta(r,r') \; 2 \, \pi \, r' \; dr' \qquad \text{for reflection} \qquad (4.2)$$

$$\Theta(r,r') = 1 \qquad\qquad 0 \le r \le r_s - r'$$

$$\Theta(r,r') = \frac{1}{\pi} \arccos \left[\frac{r'^2 + r^2 - r_s^2}{2 \, r' \, r} \right] \qquad |r_s - r'| \le r \le r_s + r'$$

$$\Theta(r,r') = 0 \qquad\qquad r > r_s + r' \quad or \quad 0 < r < r' - r_s$$

$$(4.3)$$

The last step was the calculation of the amount of light which (re)enters the sphere after diffuse illumination:

$$R_d(\text{in sphere}) = \int_0^{r_s} \Phi(r) \; 2 \, \pi \, r \; dr \qquad\qquad (4.4)$$

Table 4.3 gives the input for the different simulations for diffuse irradiation.

Table 4.3. The input parameters used for the second series of simulations. All combinations of μ_a, μ_s and g were used. 10.000 photons were launched. The critical weight equaled 0.0001.

Layer	Index of refraction	μ_a [cm^{-1}]	μ_s [cm^{-1}]	g	thickness [μm]
air	1				
glass	1.55	0.00001	0.00001	0	1000
tissue	1.37	0-5-10-15	100-150-200	0.7-0.8-0.9	500
glass	1.55	0.00001	0.00001	0	1000
air	1				

4.4 Integrating spheres

The optical properties of various dilutions of phantom materials were determined with an integrating sphere setup given in figure 4.4. Two similar setups were used: one at the Philips Research lab, Eindhoven; and one at the Laser Centre, A.M.C. Amsterdam. A general description of both set-ups will be given.
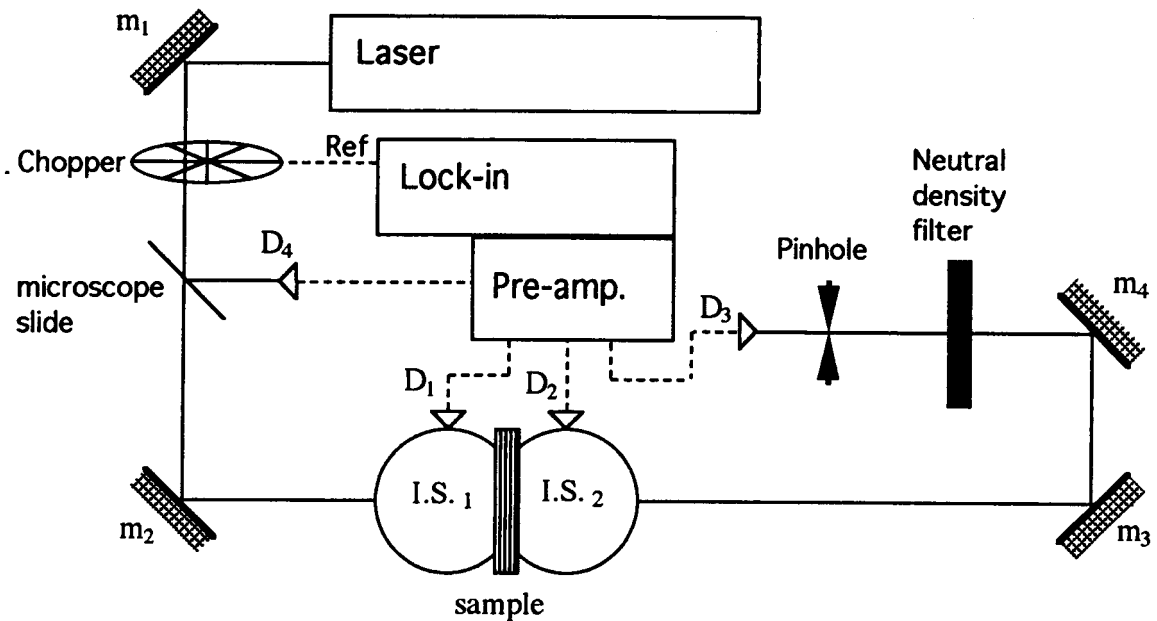
Figure 4.4. Experimental set-up used for the integrating sphere measurements. Light of a laser is chopped and directed onto a sample. The reflected and transmitted light is measured within the two integrating spheres (I.S.); the unscattered light is measured by a detector (D₃) at a large distance (≃ 2 m).

Light from a laser (Eindhoven: 5 mW HeNe, Spectra Physics, model 105-1 and a Ti:Sapphire-laser, (See section 4.5) $\lambda \simeq 780$; Amsterdam: 1 mW HeNe, Polytec, model PL650,) was chopped mechanically (Eindhoven: EG&G Princeton Applied research, model 192; Amsterdam: EG&G Princeton Applied research, model 196). A small amount of this light was tapped of by a microscope slide and measured with a detector (D_4) to make corrections for laser fluctuations possible. By use of steering mirrors (m_1 and m_2), light was directed through the reflection sphere onto the sample. The system was aligned such that the specular reflection left the reflection sphere through the entrance port. The unscattered light left the transmission sphere and was directed by two steering mirrors (m_3 and m_4) on a pinhole and was detected by a detector (D_3). The unscattered light was attenuated by a neutral density filter (O.D. 2 ⇒

attenuation of 10^{-2}). For detection photo diodes were used (D_1, D_2, D_3 and D_4) (Eindhoven: FND 100, EG&G Photon devices; Amsterdam: Telefunken, Hannover.). Since they are current sources, a current sensitive amplifier (Eindhoven: EG&G Princeton Applied research, model 184)[7] was placed between the detector and the lock-in (Eindhoven: EG&G Princeton Applied research, model 124A; Amsterdam: EG&G Princeton Applied research, model 5210).

In Eindhoven the Integrating spheres were self-made, have a low reflection factor of the sphere wall ($m \simeq 0.70$, at 633 nm) and a detector which only sees the opposite wall because it is mounted deeper into the sphere wall. In Amsterdam the Integrating spheres were made by Labsphere Inc., have a high reflection factor of the sphere wall ($m \simeq 0.97$ at 633 nm) and a baffle placed between the sample port and the detector port (see figure 3.2). The geometries of the spheres are given in table 4.4. Results of the calibration measurements are given in appendix B .

The optical properties (μ_s, μ_a and g) were reconstructed by an Inverse Adding Doubling program. This program is based on the described Adding Doubling procedure (section 2.6). The optical thickness τ was determined by measurement of the unscattered light (D_3 in figure 4.4) and reconstructed with the use of Beer's law (equation 2.13), taking into account multiple specular reflections (equation 2.19). (See appendix A) The inverse adding doubling program was written by Scott A. Prahl [22]. The program was converted by Gert W. 't Hooft [12] to run on an I.B.M. compatible p.c. and the sphere formulas (chapter 3) were implemented. Four fluxes (equation 2.35) were used to reconstruct the optical properties.

Table 4.4. The dimensions of the integrating spheres used:

Dimension:	I.S. in Eindhoven	I.S. in Amsterdam
$A = 4\pi R_c^2$	$314 \cdot 10^2$ mm^2	$729 \cdot 10^2$ mm^2
s	415 mm^2	786 mm^2
h	26.7 mm^2	147 mm^2

4.4.1 Measurement procedure

The measurements were performed in the following way:

- The system was aligned, such that the detected voltage within the integrating spheres was minimal when no sample was present. This was done with the steering mirrors m_1 and m_2 in figure 4.4.

[7] The pre-amplifier was a plug-in unit in Eindhoven. In Amsterdam the pre-amplifier was built in the lock-in.

- To determine B_1 a 99% reflectance standard was used and equation 3.18 was applied. B_2 was already known (Appendix B) (When two integrating spheres were used this was done for both spheres.)

- A sample consisted of two glass slides and a metal spacer with a drop of the solution to be investigated in between (see figure 4.5). It was mounted in such a way that all air was removed out of the spacer hole by the liquid. The sample thickness was deduced from the thickness of the two glass-slides and the thickness of the total sample.

- Either the sample was placed between the two spheres and the reflected and transmitted light was measured, or the reflected light was measured, the sphere with sample was turned around and the transmitted light was measured.

- The unscattered light was aligned (with steering mirrors m_3 and m_4) such that the signal on the third detector (D_3) was optimal. The unscattered light intensity was measured. (See figure 4.4)

- The sample was removed, the system was realigned and the total intensity was measured by D_3.

Figure 4.5. Construction of a sample.

Glass-slide
(10x5x0.05 cm)

Solution
Intralipid or Polystyrene

Metal spacer
(hole : $\varnothing = 4$ cm)

Glass-slide
(10x5x0.05 cm)
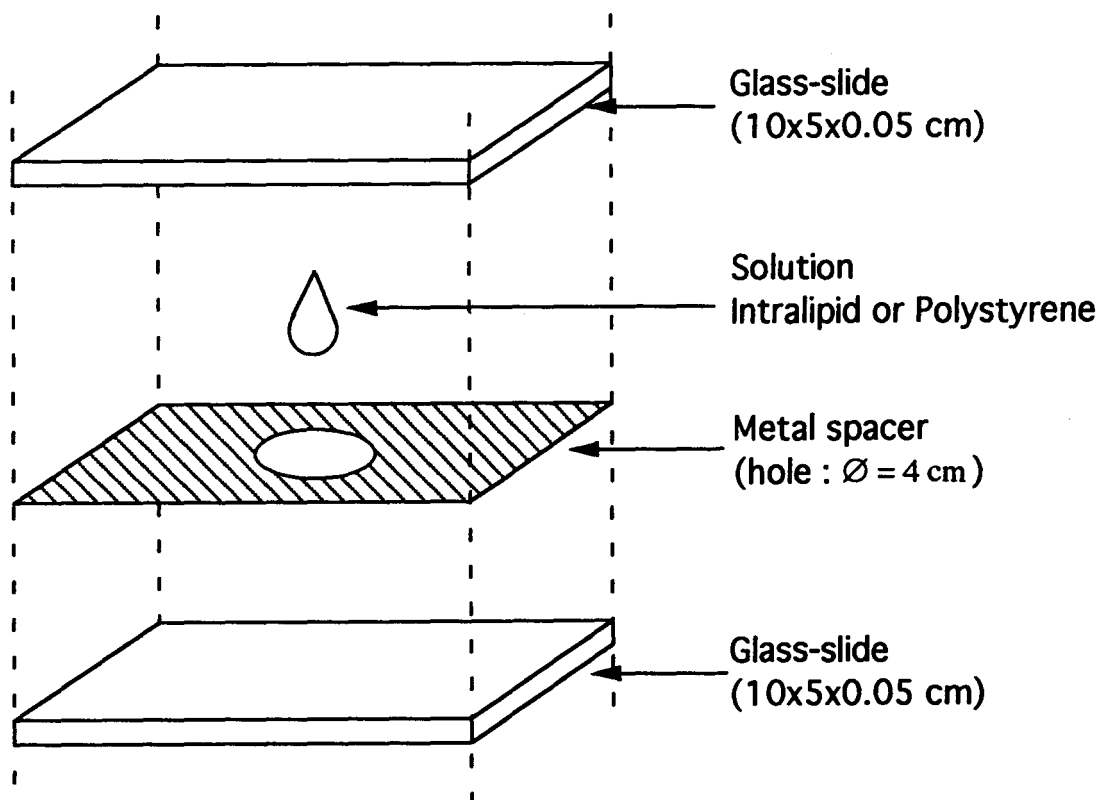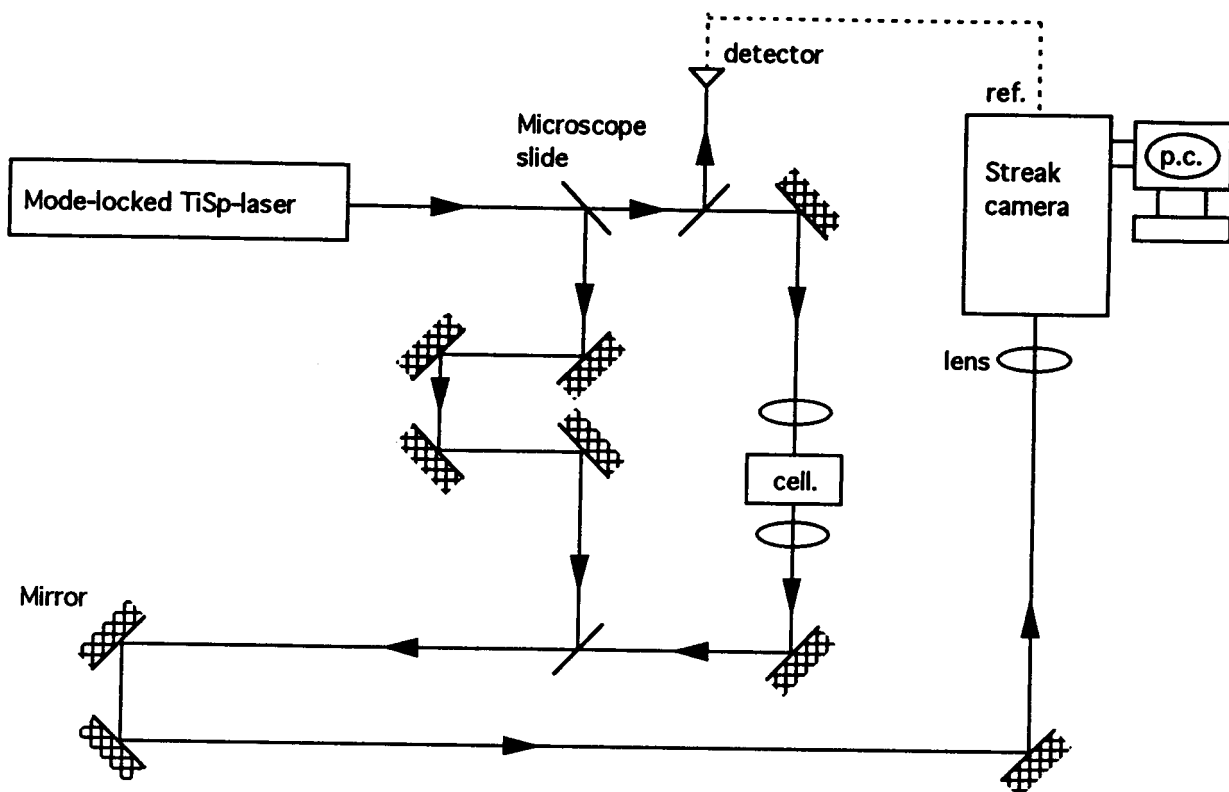
*Figure 4.6. Experimental set-up used for the time-resolved measurements. Light
of a mode-locked Ti:Sapphire laser is focused in a cell, which is filled with
one of the phantom materials. The scattered light is again focused on the
streak camera.*

*Two signals are tapped of the beam: one to trigger the streak camera
(electrical) and one to serve as a optical reference.*

4.5   Time of flight set-up

The optical properties of the various solutions were also determined with a time
resolved measurement as shown in figure 4.6. It consisted of a Ti:Sapphire-laser
mode-locking on a Kerr lens mechanism and using a HITCI saturable absorber dye jet
as a starter.[21] At the wavelength of 780 nm the average power output is 250 mW and
the pulse width is 180 fs. The repetition rate of the laser was adjusted to the
synchronization speed of the Streak camera, i.e. 82 MHz.

The light was focused in the sample, which was a cell (h x w x d = 5 x 5 x 1
cm) filled with the different dilutions. The transmitted light was focused on the
entrance slit of a Streak camera (Which was a Hamamatsu C1587 synchroscan with an

image intensified CCD camera and a streak tube with a S20 photo cathode response.). The Streak camera was triggered by a signal from a photo diode (FND 100, EG&G Photon devices), with a 82 MHz band-pass filter and amplifier (HP 8447). The laser and Streak camera combination have an instrumental resolution of 6 ps, governed by the (amplitude) stability of the trigger. The minimal integration time of the CCD camera is 1 second. The sensitivity is high enough, to detect the laser pulse easily after attenuation by an O.D. 13 filter (An attenuation of 10^{-13}.).

Part of the beam was tapped of before it passes through the sample and was also focused on the streak camera to serve as a reference.

Since the thickness of the cell is small compared to the other dimensions, an infinitely large plane parallel structure is assumed (Figure 4.7). A solution of the diffusion equation in this geometry can be found in Carslaw and Jaeger [5] where the method of multiple images is used, which results in a serie of dipoles and makes the fluence zero at z = 0 and at z = d. The resulting pulse response equals (equation 2.41):

$$T(d,z_0,t) = \frac{-\exp\left[-\mu_a c\ t\right]}{\left(\gamma^2 4\pi\ t^3\right)^{1/2}} \sum_{n=0}^{n=\infty} \left[z_{+n}\exp\left[\frac{-z_{+n}^2}{4\gamma^2\ t}\right] - z_{-n}\exp\left[\frac{-z_{-n}^2}{4\gamma^2\ t}\right] \right] \tag{4.5}$$

where

$T(d,z_0,t)$ = the transmitted, spatially integrated, intensity divided by the input intensity. [s^{-1}]

z_{+n} = $(2n + 1)d + z_0$

z_{-n} = $(2n + 1)d - z_0$

z_0 = $\dfrac{1}{\mu_s(1 - g)}$

It is assumed that the photon source is an instantaneous point source at depth z_0. This also means that the time of scattering is delayed by $t_n = z_n/c$.

The transmitted light was fit to this equation (4.5) with μ_a = 0 and the summation was made up to n = 1. So we used only two dipoles; this was considered adequate because of the term $\exp[z_n^2]$ in equation (4.5). Also the system response curve was measured (the reference).

45

z = -2d

z = -d

z = 0

z = d

z = 2d

z = 3d
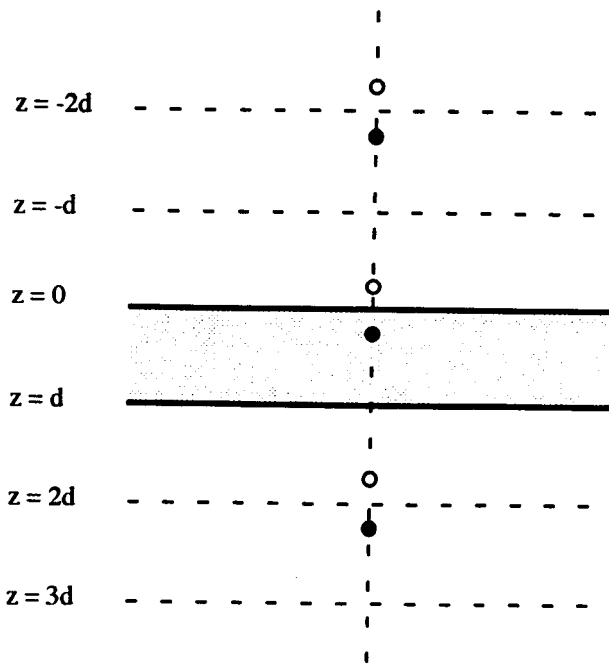
Figure 4.7. Geometry for the calculation of the time resolved reflectance and transmittance from a homogeneous slab. The boundary conditions $\phi(\rho,0,t) = 0$ *and* $\phi(\rho,d,t) = 0$ *can be met by adding an infinite serie of dipole photon sources. The first two are shown in this illustration.*
From Patterson et al.[17]

5. Results

5.1 Results of simulations

Figure 5.1 gives the output of the first series of simulations performed to investigate the light distribution within the integrating spheres after the first reflection/transmission. If the light distribution was Lambertian, then the points in the figure would lie on a horizontal line. It shows that for optically thin samples, the transmitted light is forward peaked.

Figure 5.2 gives the output of the second series of simulations performed to investigate the losses which occur, if the sample is illuminated by the sphere. It shows that losses are of the order of 10% of the total reflected light.

5.2 Results of integrating sphere measurements

Integrating sphere measurements were performed. Solutions of Intralipid$^{®}$ and Polystyrene of different concentrations were used. Measurements with the single and double integrating spheres were performed. A few important results are given below (All the results are summarized in Appendix C).

The measurements in Amsterdam did not work out. The Inverse Adding Doubling program could not find a unique set of optical properties, given the three measurements. It almost always ended at an albedo of 1, which means an absorption coefficient of 0. The measurements in Eindhoven did work out fine. Those results are presented below.

Thickness dependence

Others [2] [28] have found a thickness dependence of the total attenuation coefficient (μ_t). They have found that the scattering and absorption coefficients both decreased with increasing sample thickness. This is not found in the experiments performed here! Figure 5.3 shows the measured optical thickness as function of the physical thickness d, for different concentrations of polystyrene. The figure shows straight lines as it should be.

A thickness dependence of the absorption coefficient (μ_a) is found, μ_a decreasing as the sample thickness increases. This dependence is less in case two integrating spheres are used. This is shown in figure 5.4. Zero-values of μ_a should be considered questionable, because in such a case the inverse adding doubling program did not converge to an absolute minimum.

47

Figure 5.1. Results of Monte Carlo simulations. The angular distribution of the reflected and transmitted light. All photons were launched in the centre of the sample. (Figures 3.4b and 3.7) The sample consisted of a glass-tissue-glass geometry with different indices of refraction. The optical properties of the tissue were: a = 0.99, g = 0.8, τ = 2, 4, 8 and 16.
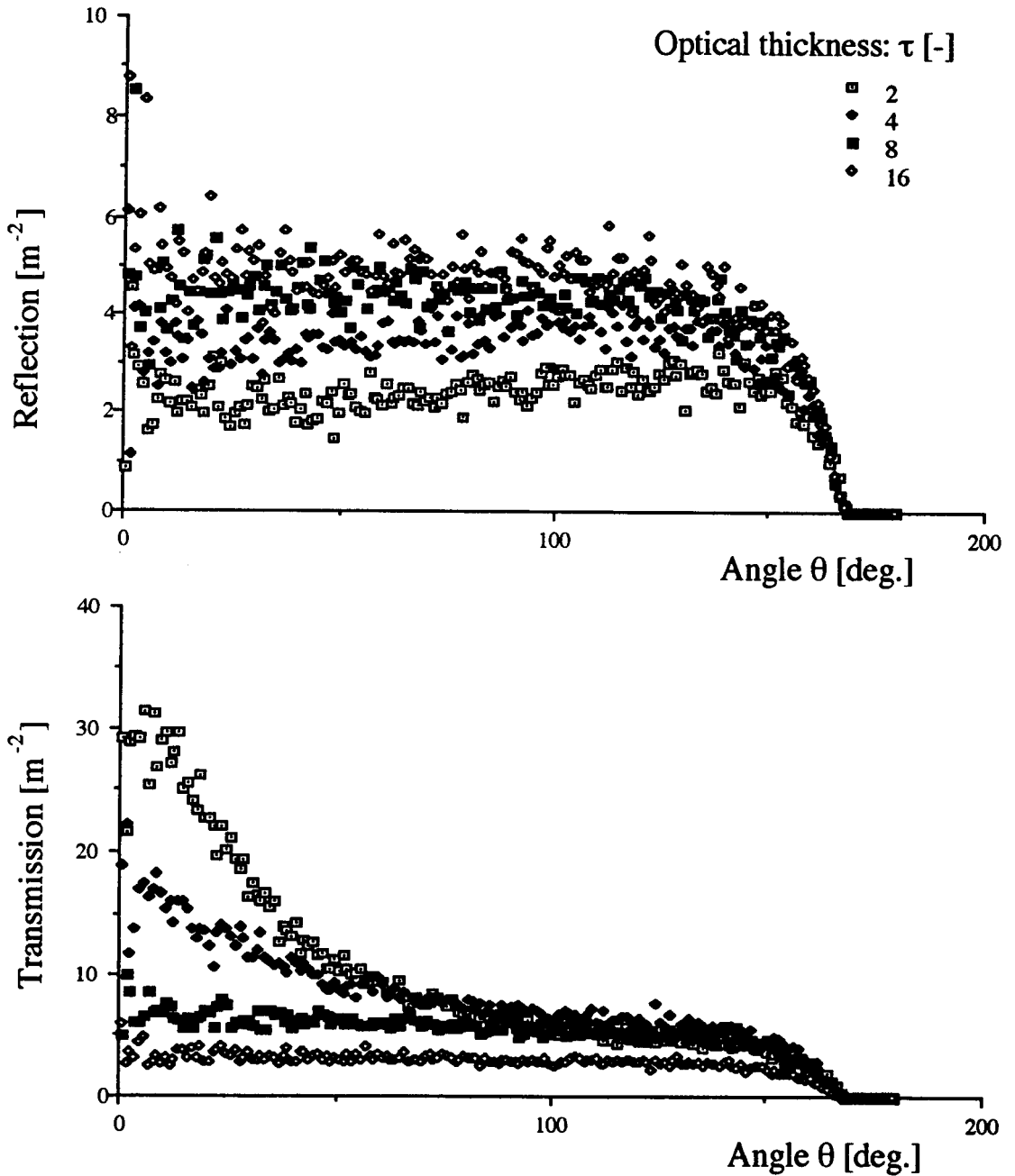
Figure 5.2. Results of Monte Carlo simulations. Percentage of R_d *and* T_d *which is lost outside the sample port, as a function of the optical properties* $(\mu'_s = \mu_s(1\text{-}g))$. *All photons were launched with a Lambertian angular distribution all over the sample port of the integrating sphere. The sample thickness was:* $d = 0.5$ *mm (exclusive the glass slides). The radius of the sample port was:* $r_s = 15.8$ *mm.*
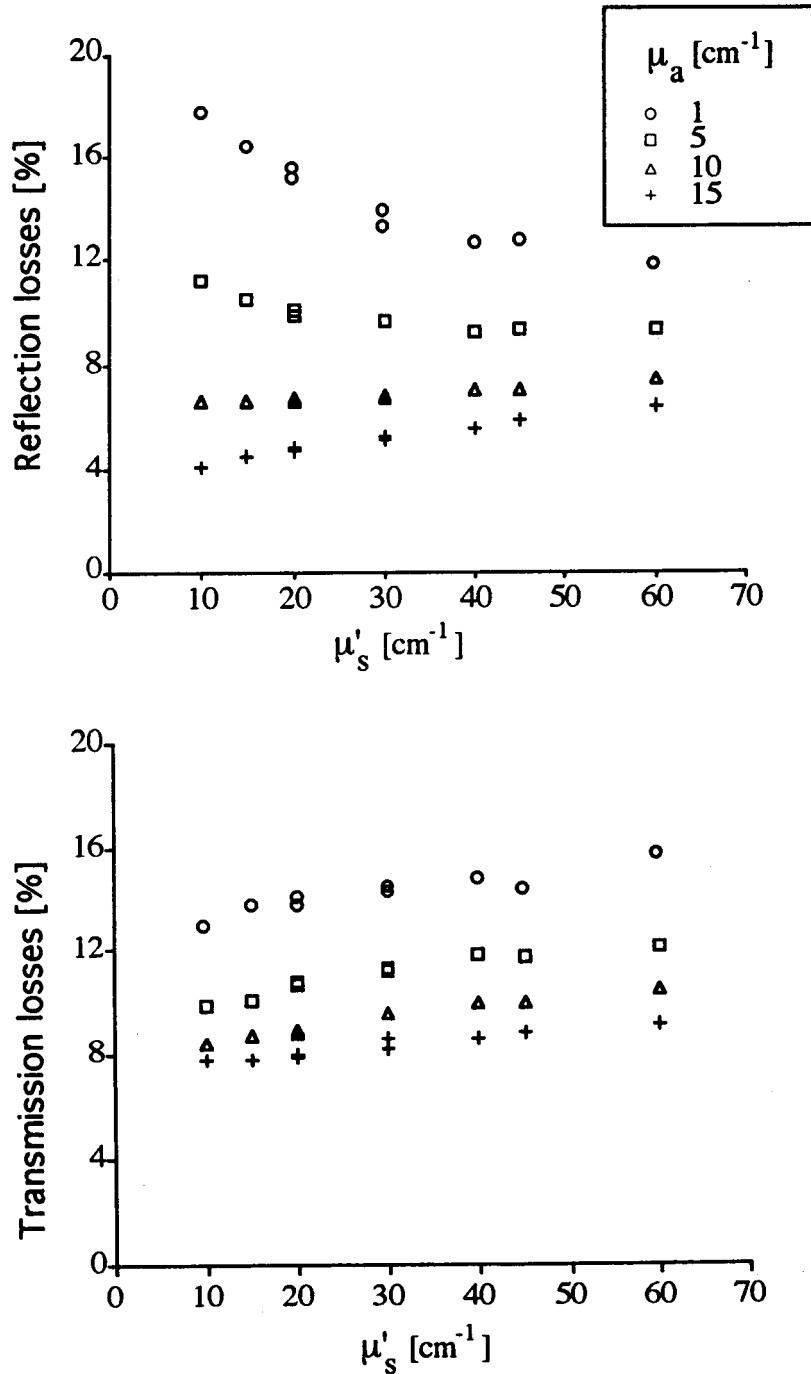
Figure 5.3. The measured optical thickness (τ) as a function of the physical thickness (d) for the different concentrations of polystyrene, at two wavelengths. The concentrations are mass concentrations. The straight lines are least squares analysis.
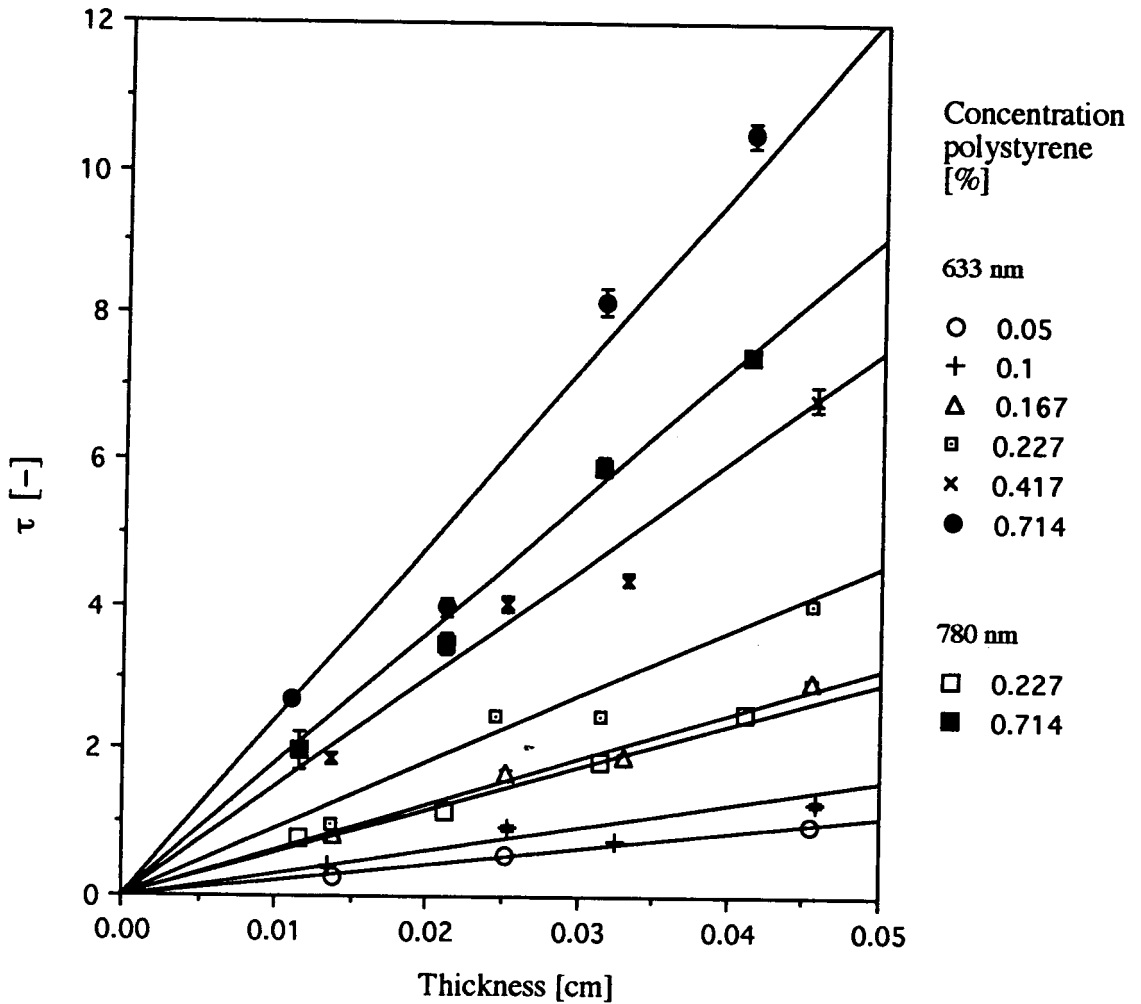
Figure 5.4. The measured absorption coefficient (μ_a) as a function of the sample thickness. Measured within double (above) and single (below) integrating spheres.
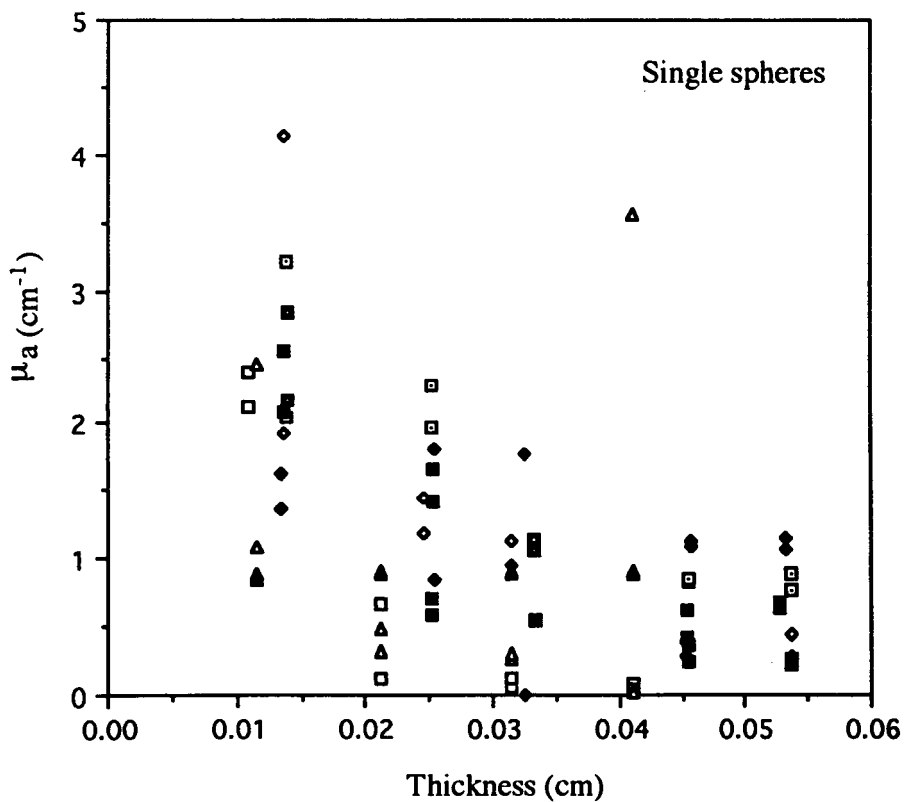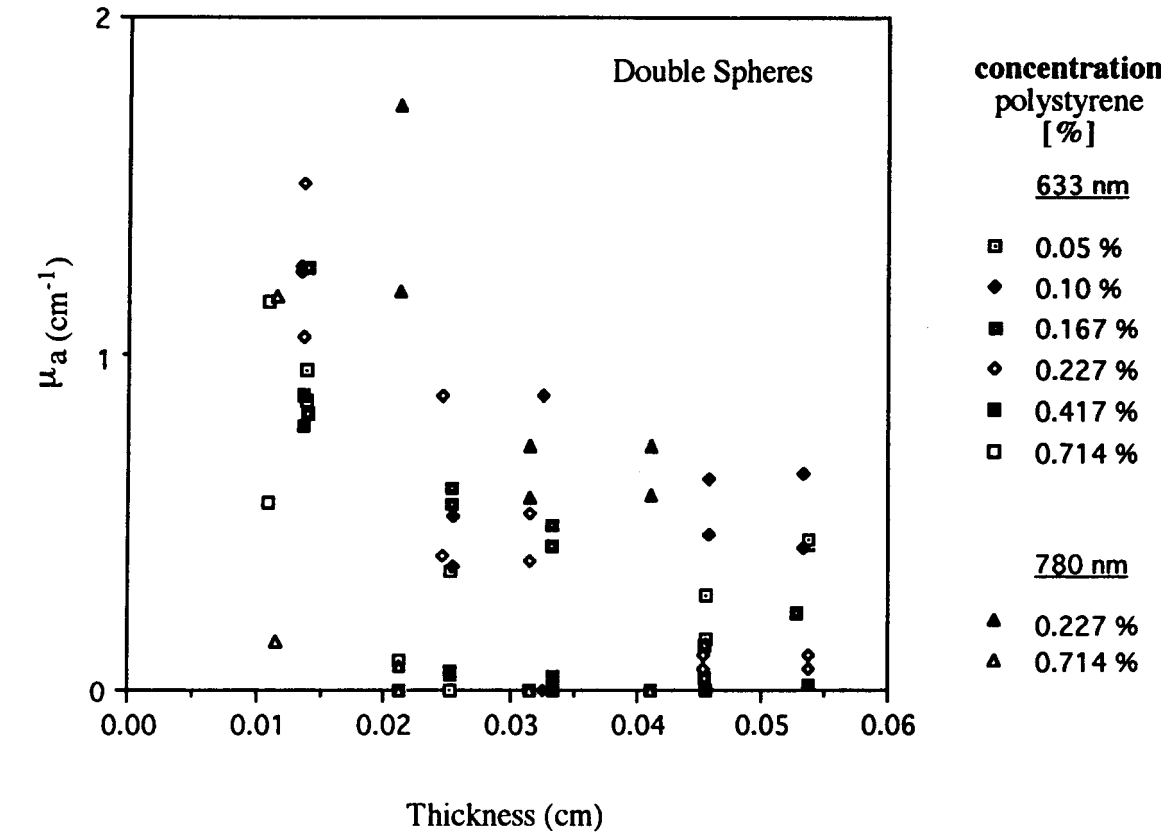
Figure 5.5 gives the results of the measured scattering coefficient of Intralipid® as a function of the concentration. Figure 5.6 compares the Mie-calculations with the measured values of μ_s of polystyrene. The scattering coefficients presented are averaged over both the different thicknesses and the double and single integrating sphere measurements (10 measurements). The error bars correspond to standard deviations. Averaging is allowed here since no relation was found between the scattering coefficient and the thickness.

There was no systematic relation found between the anisotropic factor g and the concentration and/or thickness. The measured anisotropic factor was: 0.66 ± 0.02 (at 633 nm); 0.52 ± 0.03 (at 780 nm) for Intralipid® and 0.91 ± 0.02 (at 633 nm); 0.87 ± 0.04 (at 780 nm) for polystyrene.

Figure 5.5. The measured scattering coefficient as a function of the concentration for different concentrations of Intralipid®. The straight line is found by a least squares procedure.

52
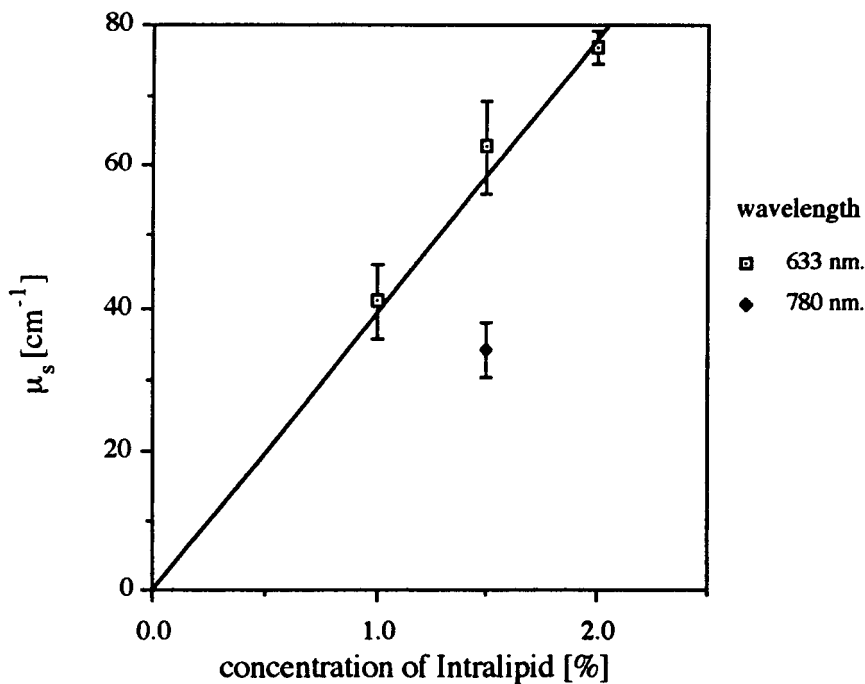
Figure 5.6. The measured scattering coefficient as a function of the concentration for different concentrations of polystyrene. The lines are calculated with Mie-theory.
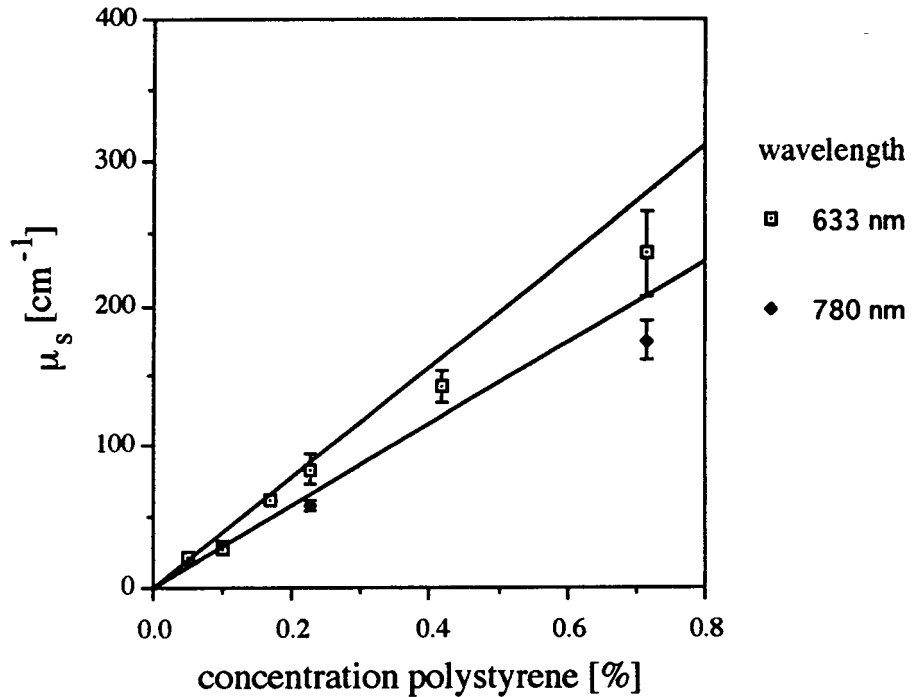
5.3   Results of time resolved measurements

Finally the Integrating sphere measurements are compared with the results obtained from time resolved measurements. This is shown in figures 5.7 and 5.8. In which the transport scattering coefficient μ_s'

$$\mu_s' = \mu_s \left(1 - g\right)$$

is plotted as a function of the concentration for the different techniques. With the time resolved measurements only one measurement was taken. Thus no error bars are printed.

Figure 5.7. The measured transport scattering coefficient as a function of the concentration of polystyrene. The lines are calculated with Mie-theory. The Integrating Sphere (I.S.) measurements are averaged over 10 measurements. The Time Of Flight (T.O.F.) measurements are single measurements.
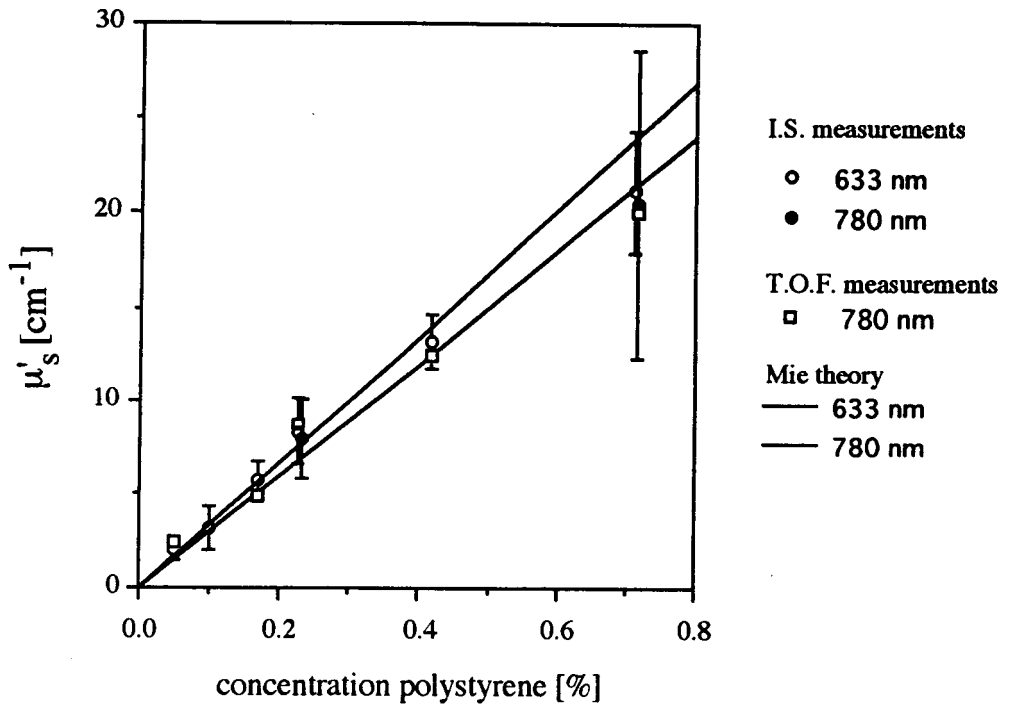
Figure 5.8. The measured transport scattering coefficient as a function of the concentration of Intralipid®. The solid lines are averages. The Integrating Sphere (I.S.) measurements are averaged over 10 measurements. The Time Of Flight (T.O.F.) measurements are single measurements.
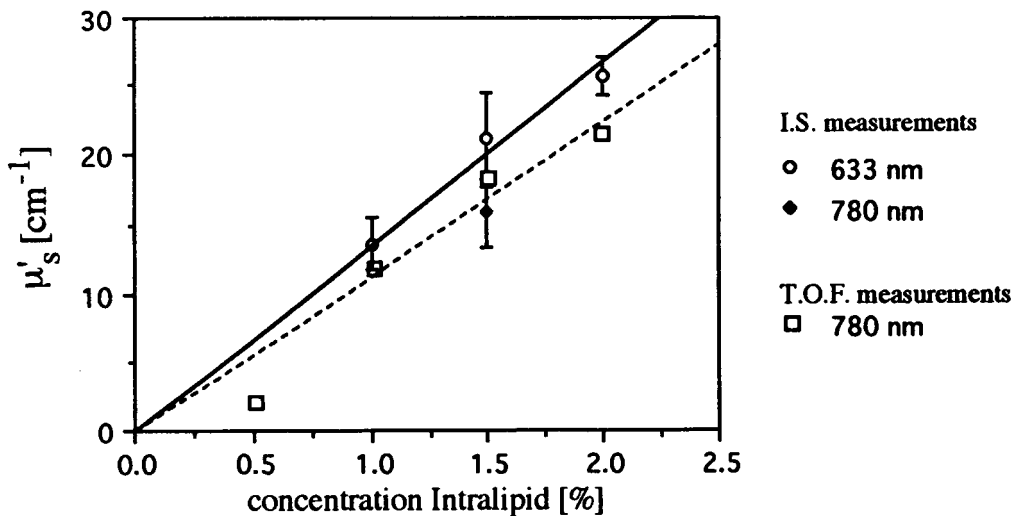
6. Discussion

Monte Carlo simulations:

The Monte Carlo program used was tested by comparing reflected and transmitted intensities with results from the Adding Doubling program. The reflection and transmission coefficients agreed well within 1 to 2 %.

The Monte Carlo simulations performed showed two features. The light distribution in transmission is forward peaked. (Figure 5.1.) and losses occur to the sides of the sample (Figure 5.2). Both features influence the accuracy of the optical properties determined with the use of integrating spheres.

In case the light distribution, leaving the sample, is forward peaked, more light is lost through the exit port than is theoretically accounted for. Since the solid angle of the exit port in the integrating sphere is very small, this is only a minor effect.

Also the light distribution, within the integrating sphere, is not uniform. This means that the detector can receive more or less light (than is theoretically accounted for) depending on which part of the sphere is seen by the detector. In case of a non-isotropic detector (Eindhoven), the detector "sees" a part of the opposite sphere wall. In case of a baffle (Amsterdam), the detector "sees" merely an area around the exit/entry port than around the sample port. So more light is measured than is assumed with a Lambertian emitting sample. If the light distribution within the integrating sphere is not uniform, the sample will not be uniformly illuminated by the sphere.

If losses occur at the sides of the sample, the absorption coefficient μ_a determined will be too high, because the reconstruction algorithm assumes that all reflected and transmitted light is measured. These losses are a higher order effect, because they relate to the diffuse illumination of the sample by the sphere and not to the collimated incident irradiation. Within a "good" integrating sphere (i.e. one with a high diffuse reflection factor of the sphere wall) this influence on the absorption coefficient will be higher than within a "bad" quality integrating sphere. From figure 5.2 it follows that the largest losses appear for samples with the lowest absorption coefficients.

Our Monte Carlo simulations don not predict a thickness dependence of the total attenuation coefficient, because the reconstruction of the total attenuation

coefficient is based on the same principles which are used within the Monte Carlo method.

We still don not know which method is the best to measure the unscattered light and to use this to reconstruct the optical thickness. We have chosen to place the sample perpendicular to the incident laser beam. This is done to minimize the displacement of the unscattered reflected and transmitted light, so that they can indeed leave the entry and exit port of the integrating sphere(s). Due to this configuration interference effects may appear due to multiple reflections. However these effects are small because 95% of the incident light (first transmission through the first glass slide) should interfere with 0.02 % of the incident light (second transmissions through the glass slide). The influence of both glass slides on each other will be negligible with thick samples.

Integrating sphere measurements:

With the measurement technique used (by realigning the unscattered light every time a sample is placed in to or out of the beam) we failed to measure thickness dependencies. If this realigning is not performed, then it is highly likely that a lower unscattered intensity will be measured. (This will result in a higher optical thickness). This artifact becomes more important for thicker samples, thus a thickness dependence can occur in this way. If the sample is not placed perpendicular to the incident beam and the optical thickness is reconstructed with the using multiple reflections, a thickness dependence is also introduced.

Figure 5.3. shows no thickness dependence of the total attenuation coefficient. Figure 5.4. shows that the absorption coefficient does decrease with increasing thickness. Also the variation in the values of μ_a measured decreases with increasing thickness. The absorption coefficients measured with the double integrating spheres are approximate half the values measured with the single integrating spheres.

In case the other optical properties (μ_s and g) are known, the absorption coefficient is reconstructed in the following way. The average distance travelled within the sample ($<\ell>$), due to scattering, is calculated (without absorption). The total amount of light leaving the sample, after one reflection, is calculated by summing up all reflection and transmission coefficients. The losses which occur after one reflection/transmission are calculated ($\sum$ losses = 1 - $\sum$ reflection coefficients - $\sum$ transmission coefficients). The absorption coefficient is reconstructed with the use of Beer's law:

$$\sum \text{losses} = 1 - e^{-\mu_a <\ell>} \qquad \Rightarrow \qquad \sum_i R_i + \sum_i T_i = e^{-\mu_a <\ell>}$$

All the features in figure 5.4. can be understood with use of this simple formula. Losses to the sides of the sample (found by the Monte Carlo simulations) increase the term on the left hand side, thus they will result in the prediction of a higher absorption coefficient. With increasing sample (or optical) thickness the average distance travelled within the sample $<\ell>$ increases, while the losses, to the sides of the sample, remains unchanged. This will result in a lower (reconstructed) absorption coefficient.

From this equation it also follows that increasing the sample thickness (and hence increasing $<\ell>$) will result in a decrease of the variation of the absorption coefficient. Because while $<\ell>$ increases, the variation in the losses remains unchanged.

To understand why double integrating spheres determine a lower absorption coefficient, the non-uniform light distribution within the transmission sphere has to be used too. This light distribution will be responsible for a non uniform re-illumination of the sample and since the transmission coefficient is higher for illumination under small angles ($T_{cd} > T_d$), this illumination will give a stronger interaction between the two spheres than is accounted for. Thus more light intensity is measured and losses seem less in case two integrating spheres are used. If the sample is less forward peaked (thicker samples and/or lower g-factor) this effect is smaller.

This effect is also held responsible for the fact that the integrating sphere measurements in Amsterdam did not give reliable results. It is because the detector sees that part of the sphere surface which does receive the most light. Thus the intensity measured is higher than with a Lambertian sample. The high reflectance factor of the sphere wall does magnify this effect.

From figures 5.5 and 5.6 it follows that the scattering coefficient increases proportional with the concentration of scatters, at high concentrations this seems not valid anymore. The explanation can be that the scattering events are no longer independent. But the criterion of Van de Hulst (Footnote 1 page 4) is not violated. For a concentration of 1 %, the distance between the particles is on the average 8 times the particle diameter ø. (For 2.5% they are on the average 6 times the particle diameter away from each other). But the question whether or not the

scattering events are independent should be related to the type of experiments performed. The average distance between the particles is large enough to talk about one phase function (in case that polystyrene is used). But in an attenuation experiment one measures the probability of light to be scattered over a large distance (d $\simeq$ 300 ø), in which case the scattering events may not be considered independent any longer.

Time resolved measurements:

The results of the effective scattering coefficient obtained from the time resolved measurements are in agreement with the values obtained from the integrating sphere measurements. The best fits of the time resolved data, with time dependent diffusion theory, were achieved with the highest concentration of scatters. For low concentrations the width of the detected time resolved peak came in the order of the width of the original (reference) pulse. In such a case the fit could slightly by improved by convolving the theoretical curve with the reference pulse (the systems response curve).

7. Conclusions

It is possible to measure optical properties of tissue with integrating spheres in combination with an Inverse Adding Doubling reconstruction algorithm. However, attention has to be given to the following subjects:

The integrating sphere does not need to have a high reflectance factor of the sphere wall. In fact, the best integrating sphere is a "bad integrating" sphere. The detector has to be placed such that it receives light from a representative part of the integrating sphere wall, but not from the sample. (A baffle should be avoided, because this disturbs the sphere geometry). This has to be done properly in order to deal with non-Lambertian samples.

Care has to be taken with the measurement of the unscattered light. Optically thick samples are preferred ($\tau \in$ (4,8)). Optically thin samples should be avoided because they lead to a too high absorption coefficient. Thick samples should be avoided because the unscattered light will virtually impossible to be measured.

Table 7.1. Results of the measurements performed. (At two wavelengths)

The scattering is assumed to vary linearly with the concentration: $\mu_s = \mu_{so}$ *concentrations.*

The concentration is given in mass percentage [% g/g].

The absorption coefficient is caused by losses within the integrating sphere.

Polystyrene   **Intralipid®**

632.8 nm	Mie theory	Integrating Spheres	Integrating Spheres
μ_{so} [cm^{-1} %$^{-1}$]	389.6	346 ± 55	40 ± 4
μ_a [cm^{-1}]	0.0	0.4 ± 0.4	1.2 ± 0.9
g [-]	0.914	0.91 ± 0.02	0.66 ± 0.02
μ'_{so} [cm^{-1} %$^{-1}$]	33.49	34 ± 6	14 ± 1

780 nm	Mie theory	Integrating Spheres	Time resolved	Integrating Spheres	Time resolved
μ_{so} [cm^{-1} %$^{-1}$]	289.3	256 ± 20	-	23 ± 2	-
μ_a [cm^{-1}]	0.0	2 ± 2	-	2 ± 2	-
g [-]	0.896	0.87 ± 0.04	-	0.52 ± 0.03	-
μ'_{so} [cm^{-1} %$^{-1}$]	29.98	25 ± 9	31 ± 5	11 ± 1	10 ± 3

Low absorption coefficients cannot be measured within the method described! It seems reasonable to predict that it is possible to measure high absorption coefficients, but this has to be investigated further.

The values measured of the optical properties are given in table 7.1

Beek [2] has found for Intralipid at 632.8 nm:

μ_{so} = 56.1 ± 2.8 cm^{-1}/(ml/L); g = 0.70 ± 0.05.

Van Staveren et al.[26] have found:

μ_{so} = 47.6 ± 0.6 cm^{-1}/(ml/L); g = 0.768 ± 0.006; μ_{ao} = 0.0149 ± 0.0004 cm^{-1}/(ml/L); (at 633 nm) and

μ_{so} = 13.1 ± 0.3 cm^{-1}/(ml/L); μ_{ao} = 0.48 ± 0.09 cm^{-1}/(ml/L); (at 1064 nm)

Flock et al.[8] have found

μ_{so} = 34 ± 3 cm^{-1}/(ml/L); g = 0.825; μ_{ao} = 0.00013 cm^{-1}/(ml/L); (at 633 nm)

8. References

1   S.R. Arridge, M. Cope and D.T. Delpy, "The theoretical basis for the determination of optical pathlengths in tissue: temporal an frequency analysis," Phys. Med. Biol., Vol. 37, No. 7, pp. 1531-1560, 1992.

2   J.F. Beek, "Pneumothorax monitoring by remittance measurement," Ph.D. thesis at the University of Amsterdam, 1993.

3   B. Chance (editor), "Photon Migration in Tisssues," Plenum press, New York and London, 1989.

4   P.F. O'Brien, "Network Representation of the Integrating Sphere," J.Opt. Soc. Am., Vol. 46, No. 5, pp. 343-345, 1956.

5   H.S. Carslaw and J.C. Jaeger, "Conduction of Heat in Solids," (Second edition), Clarendon, Oxford, 1986.

6   M. Essenpreis, "Thermally Induced Changes in Optical Properties of Biological Tissues," Ph.D. thesis of the University of London, 1992.

7   J.B. Fishkin and E. Gratton, "Propagation of photon-density waves in strongly scattering media containing an absorbing simi-infinite plane bounded by a straight edge," J. Opt. Soc. Am. A, Vol. 10, No 10, pp. 127-140, 1993.

8   S.T. Flock, S.L. Jacques, B.C. Wilson, W.M. Star, and M.J.C. van Gemert, "Optical Properties of Intralipid: A Phantom Medium for Light Propagation Studies," Lasers Surg. Med. 12, pp. 510-519, 1992.

9   P.M.E.M v.d. Grinten, "Prisma-Technica 40: Procesregelingen", Het Spectrum n.v., Utrecht.

10 J.C. Hebden and R.A. Kruger, "Simulating the performance of a time-of-flight transillumination imaging system" SPIE Vol. 1205, pp. 142-149, 1990.

11 E. Hecht, "Optics," (Second edition), Addison-Wesley publishing company, Inc. (1987).

12 G.W. 't Hooft, D.G. Papaioannou, J.J.M. Baselmans, M.J.C. van Gemert, "Dependence of image quality on optical parameters in time-resolved transillumination experiments." Proc. of the SPIE, Budapest, 1993.

13 H.C. van de Hulst, "Light Scattering by Small Particles," Dover Publications, Inc. New York, 1957.

14 S.L. Jacques, L. Wang "Monte carlo simulations," book-chapter editors: M.J.C. van Gemert and S.A. Prahl, to be published.

15 S.J. Mason, "Feedback Theory - Further Properties of Signal Flow Graphs," Proc. IRE (IEEE), Vol. 44, p. 920 - 926, 1956.

16 R. Meijerink, "Optical changes of heated egg white and agg yolk and denaturation and aggregation of the molecules," internal report, Laser Centre, A.M.C. Amsterdam, 1993.

17 M.S. Patterson, B. Chance and B. C. Wilson, "Time resolved reflectance and transmittance for the noninvasive measurement of tissue optical properties," Applied optics, Vol 28, No. 12, pp. 2331-2336, 1989.

18 M.S. Patterson, B.C. Wilson, D.R. Wyman, "The Propagation of Optical Radiation in Tissue I. Models of Radiation Transport and their Application," Lasers in Medical Science, Vol. 6, pp. 155-168, 1990.

19 J.W. Pickering, C.J.M. Moes, H.J.C.M. Sterenborg, S.A. Prahl and M.J.C. van Gemert. "Two integrating spheres with an intervening scattering sample," J. Opt. Soc. Am. A., Vol. 9, pp. 621 - 631, 1992.

20 J.W. Pickering, S.A. Prahl, N. van Wieringen, J.F. Beek, H.J.C.M. Sterenborg, M.J.C. van Gemert, "Double integrating sphere system for measuring the optical properties of tissue," Applied Optics, Vol. 32, pp. 399-410, 1993.

21 N. Sarukura, Y. Ishida and H. Hakano, "Generation of 50-fsec pulses from a pulse-compressed, cw, passively mode-locked Ti:sapphire laser," Optics Letters, Vol. 16, No. 3, pp. 153-155, 1991.

22 S.A. Prahl, "A User's Manual for the Inverse Adding-Doubling Program," May 7, 1991.

23 S.A. Prahl, "Light transport in Tissue," Ph.D. thesis of the University of Texas at Austin, 1988.

24 S.A. Prahl, M.J.C. van Gemert and A.J. Welch, "Determining the optical properties of turbid media by using the adding-doubling method," Applied Optics, Vol. 32, pp. 399-410, 1993.

25 W.M. Star and S.A. Prahl, "Diffusion Approximation," book-chapter editors: M.J.C. van Gemert and S.A. Prahl, to be published.

26 H.J. van Staveren, C.J.M. Moes, J. van Marle, S.A. Prahl and M.J.C. van Gemert, "Light scattering In Intralipid-10% in the wavelength range of 400-1100 nm," Appl. Opt. Vol. 31, No. 31, pp. 4507-4514, 1991.

27 O. Tian Tan, "Investigation and Optimization of Laser Treatment of Portwine Stains," Ph.D. thesis at the University of Amsterdam, 1993.

28 H. Vijverberg, "Determination of the relationship between sample thickness and optical properties using a double integrating sphere setup," internal report, Laser Centre, A.M.C. Amsterdam, 1991.

29 N. van Wieringen, "The limitations of the determination of optical properties of tissue with a double integrating sphere set-up," internal report, Laser Centre, A.M.C. Amsterdam, 1990.

30 W.J. Wiscombe, "On initialization, error and flux conservation in the doubling method," J. Quant. Spectrosc. Radiat. Transfer, Vol. 16, pp. 637-658, 1976.

Appendix A:

Collimated reflection en transmission coefficients:

In this appendix the "collimated" reflection and transmission coefficients are derived with the use of signal flow graphs. A five-layer geometry is assumed: air, glass, tissue, glass and air. These layers are plane parallel and light is incident perpendicular at the first layer. See figure A.1. The reflection and transmission coefficients are derived from scattering and absorption of the second layer.
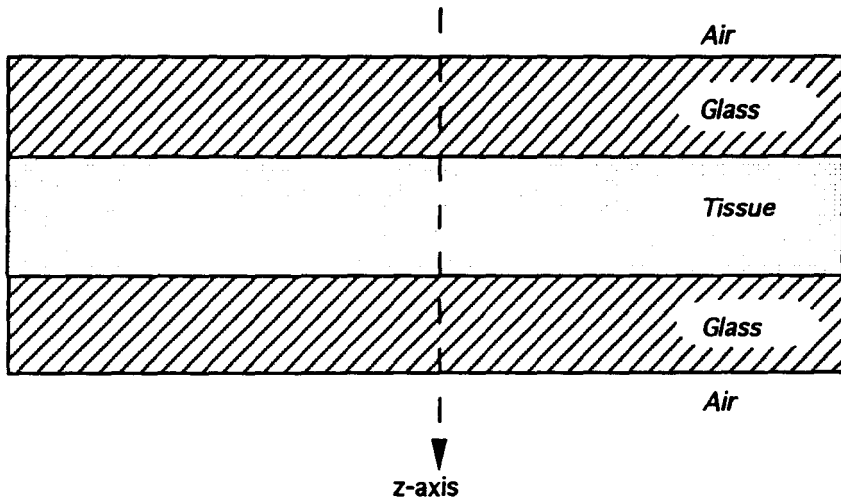
Figure A.1. The five layer structure used in the calculations.

The reflection and transmission coefficients for one boundary are determined by the laws of Fresnel. These laws are for normal incidence [11]:

$$R_{12} = \left(\frac{n_1 - n_2}{n_1 + n_2} \right)^2 \tag{A.1}$$

where

R_{12} is the reflection coefficient for normal incidence.

n_1 is the index of refraction of the incident medium.

n_2 is the index of refraction of the transmitted medium.

All the interfaces reflect light. Light reflected by all the interfaces is a sum of multiple reflections.

It is assumed that in the tissue unscattered light propagates according to Beers' Law:

$$I(z) = I_o \exp\left[- \mu_t z\right] \qquad\qquad (A.2)$$

where

I(z) is the light intensity at depth z,

I_o is the light intensity at z = 0,

μ_t is the total attenuation coefficient ($\mu_t = \mu_a + \mu_s$).

The product μ_t z is often referred to as the optical thickness τ.

This means that when light propagates through the tissue layer, its gain is $e^{-\tau}$.
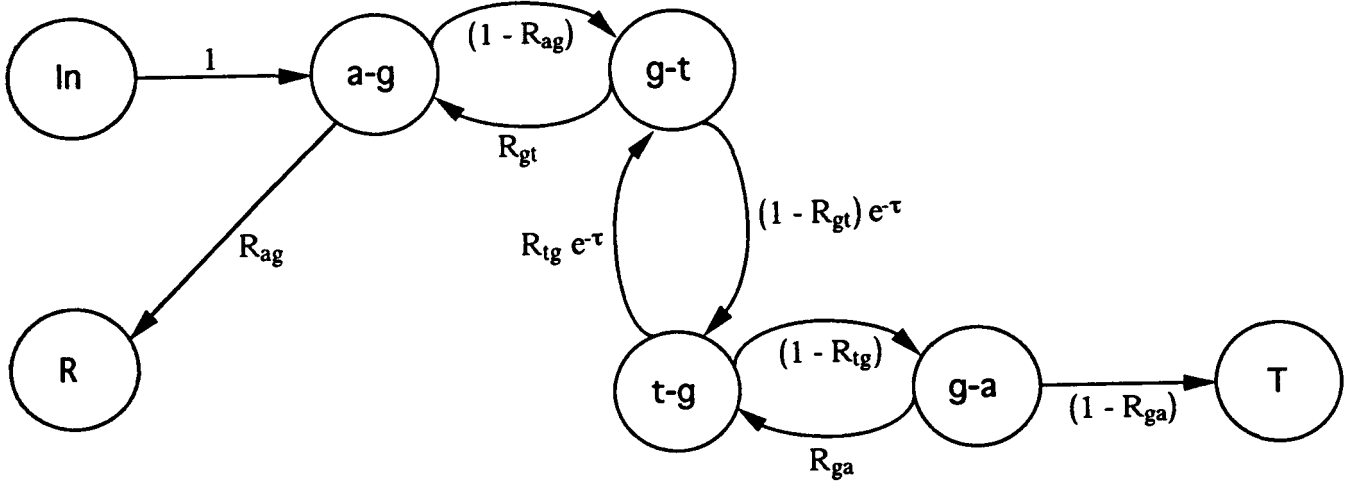
Figure A.2. Signal flow graph for the calculation of R_c *and* T_c.

The nodes represent the boundaries between:

air - glass - tissue - glass -air.

For the transmission and reflection of the total geometry the signal flow graph of figure A.2 can be made, in which the nodes represent the boundaries. With the use of this figure and the use of equation 3.3 the total transmission and reflection can be derived.

$$T = \frac{\left(1-R_{ag}\right)\left(1-R_{gt}\right)\exp\left[-\tau\right]\left(1-R_{tg}\right)\left(1-R_{ga}\right)}{1-\left(1-R_{ag}\right)R_{gt}-\left(1-R_{gt}\right)R_{tg}\exp\left[-2\tau\right]-\left(1-R_{tg}\right)R_{ga}+\left(1-R_{ag}\right)R_{gt}\left(1-R_{tg}\right)R_{ga}}$$ (A.3)

$$R = \frac{R_{ag}\left[1-\left(1-R_{gt}\right)R_{tg}\exp\left[-2\tau\right]-\left(1-R_{tg}\right)R_{ga}\right]}{1-\left(1-R_{ag}\right)R_{gt}-\left(1-R_{gt}\right)R_{tg}\exp\left[-2\tau\right]-\left(1-R_{tg}\right)R_{ga}+\left(1-R_{ag}\right)R_{gt}\left(1-R_{tg}\right)R_{ga}}$$ (A.4)

Where the subscripts indicate the following
- the first subscript is the incident medium,
- the second subscript is the adjacent medium.

a = air;

g = glass;

t = tissue;

With the use of $X_{xy} = X_{yx}$ these equations become:

$$T = \frac{\left(1-R_{ga}\right)^2\left(1-R_{gt}\right)^2\exp\left[-\tau\right]}{1-\left(1-R_{ga}\right)R_{gt}-\left(1-R_{gt}\right)R_{gt}\exp\left[-2\tau\right]-\left(1-R_{gt}\right)R_{ga}+\left(1-R_{ga}\right)R_{gt}\left(1-R_{gt}\right)R_{ga}}$$ (A.5)

$$R = \frac{R_{ga}\left[1-\left(1-R_{gt}\right)R_{gt}\exp\left[-2\tau\right]-\left(1-R_{gt}\right)R_{ga}\right]}{1-\left(1-R_{ga}\right)R_{gt}-\left(1-R_{gt}\right)R_{gt}\exp\left[-2\tau\right]-\left(1-R_{gt}\right)R_{ga}+\left(1-R_{ga}\right)R_{gt}\left(1-R_{gt}\right)R_{ga}}$$ (A.6)

The denominator can be written as:

$$\left[1-\left(1-R_{ga}\right)R_{gt}\right]\left[1-\left(1-R_{gt}\right)R_{ga}\right]-\left(1-R_{gt}\right)R_{gt}\exp\left[-2\tau\right]$$ (A.70

Formally this equation is not correct, because it is not allowed to sum light *intensities*. It is only allowed to sum over *amplitudes*. This can be done with the use of complex amplitudes.
When light travels from one boundary to the other, the gain should be multiplied by

$$e^{-i\phi_m} \qquad\qquad\qquad (A.8)$$

to correct for the phase delay.

(ϕ_m = phase delay, m = medium through which light travels)

Also reflection factors for amplitudes should be used:

$$r_{12} = \frac{n_1 - n_2}{n_1 + n_2} \qquad\qquad (A.9)$$

The amplitude transmission factor becomes:

$$t = \qquad\qquad\qquad (A.10)$$

$$\frac{\left(1-r_{ag}\right)\left(1-r_{gt}\right)e^{-\tau/2-i(\phi_t+\phi_{g1}+\phi_{g2})}\left(1-r_{tg}\right)\left(1-r_{ga}\right)}{1-\left(1-r_{ag}\right)r_{gt}e^{-2i\phi_{g1}} -\left(1-r_{gt}\right)r_{tg}e^{-\tau-2i\phi_t} -\left(1-r_{tg}\right)r_{ga}e^{-2i\phi_{g2}} +\left(1-r_{tg}\right)r_{ga}\left(1-r_{ag}\right)r_{gt}e^{-2i(\phi_{g1}+\phi_g)}}$$

with ϕ_{g1}, ϕ_{g2}, $\phi_t \in [0, 2\pi)$

If one assumes that the phases are random, than an average transmission can be calculated as:

$$< T > = < t\, t^* >$$

Appendix B:

Results of calibration measurements:

Two types of integrating spheres are used. They both are calibrated with the use of reflection standards (made by Labsphere). The reflection values are given in table B.1.

The results of the calibration are given in figures B.1, B.2, B.3 and B.4.

Table B.1. Reflection values of the reflection standards used.

number	value [%] (at 633 nm)	value [%] (at 780 nm)
99	96.95 ± 0.06	98.4 ± 0.6
75	74.85 ± 0.03	75.3 ± 0.3
50	54.82 ± 0.01	54.8 ± 0.1
2	2.7361 ± 0.0002	2.897 ± 0.002

Figure B.1. and B.2. The results of calibration measurements performed with the spheres in Eindhoven. The linear fit is to determine the sphere constants: B_1 *and* B_2 *by use of equation (3.21).*
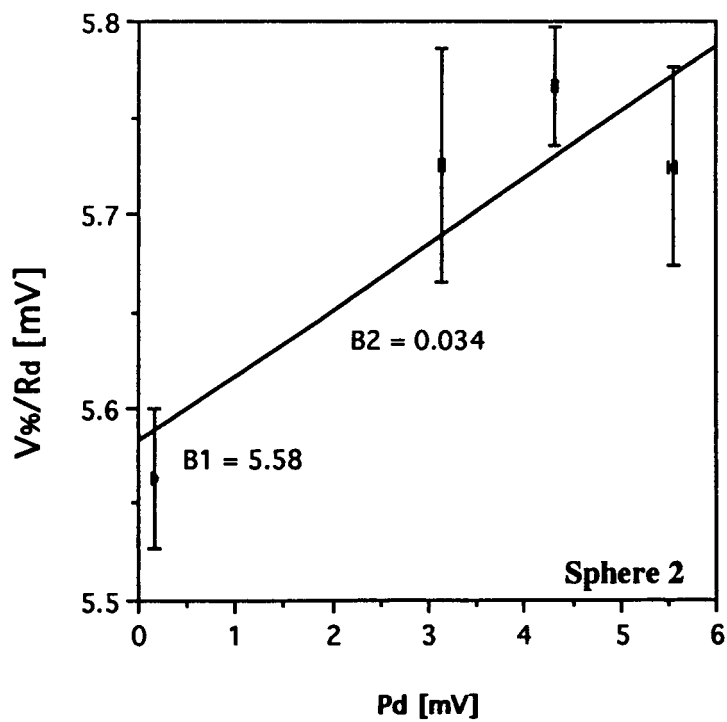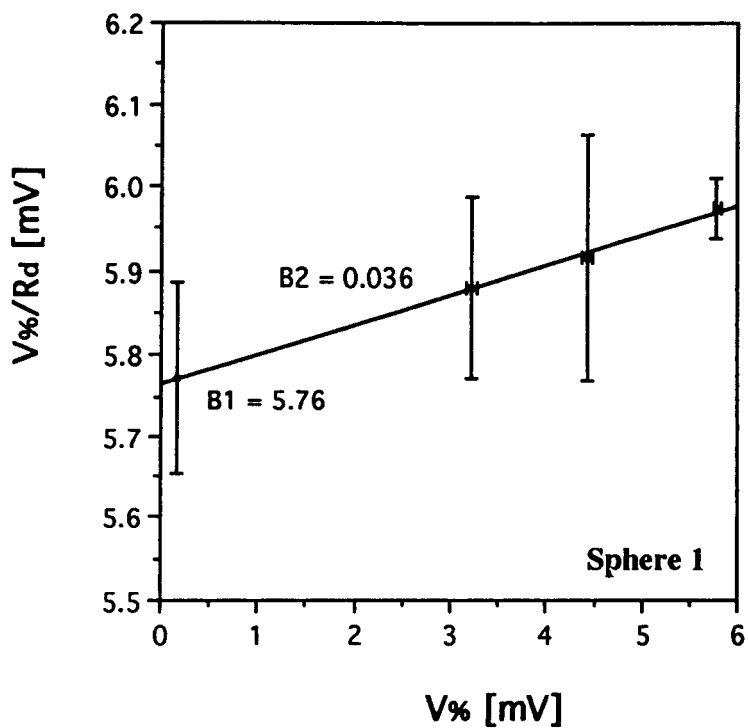
Figure B.3. and B.4. The results of calibration measurements performed with the spheres in Amsterdam. The linear fit is to determine the sphere constants: B_1 *and* B_2 *by use of equation (3.21).*
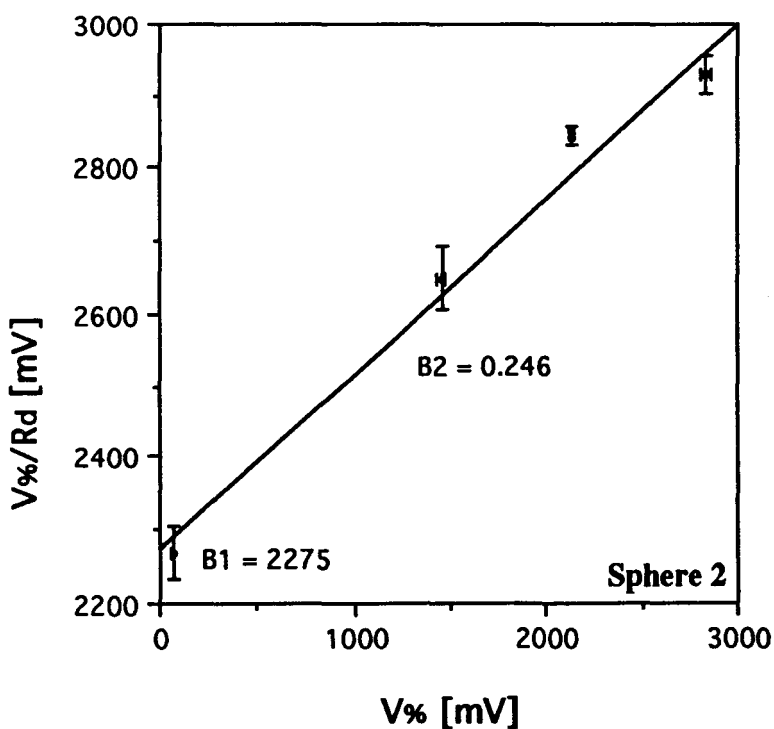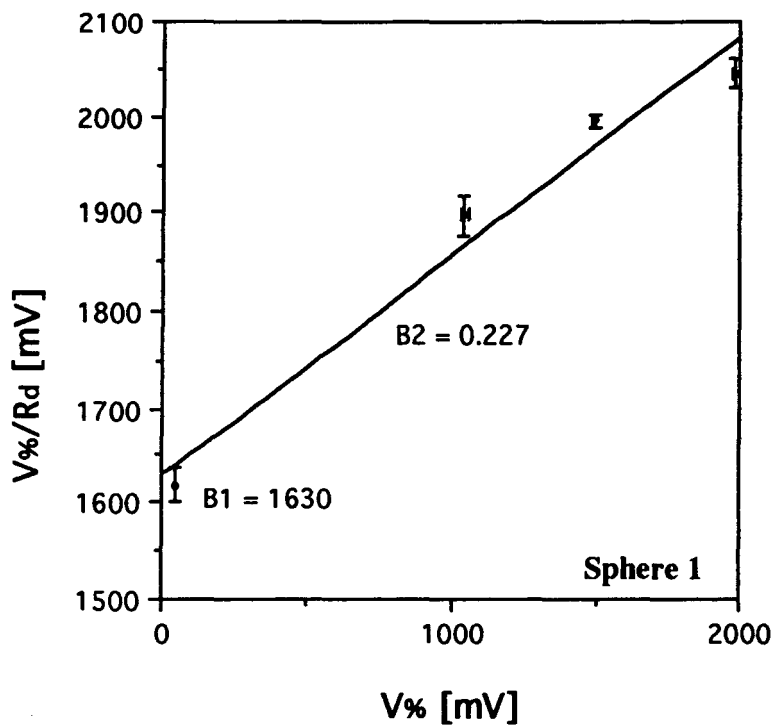
Appendix C:

Results of Integrating sphere measurements

Intralipid two Integr. Spheres

concentration	wavelength	thickness	opt. thickness	g	mu_a	mu_s
[%]	[nm]	[cm]	[-]	[-]	[cm-1]	[cm-1]
1	632.8	0.0112	0.5017	0.639	2.8529	41.9373
1	632.8	0.0163	0.5512	0.6762	0.2033	33.6149
1	632.8	0.0223	0.9292	0.6442	1.2462	40.4231
1	632.8	0.026	1.2648	0.6611	1.6247	47.0216
1	632.8	0.032	1.4946	0.6638	1.0275	45.6773
1	632.8	0.0113	0.4444	0.6504	1.3888	37.9424
1	632.8	0.0147	0.6364	0.6404	1.5352	41.7548
1	632.8	0.0216	0.8827	0.6434	1.1035	39.7625
1	632.8	0.0261	1.0199	0.6552	0.3693	38.7064
1	632.8	0.033	1.3292	0.6619	0.5274	39.7507
1.5	632.8	0.012	0.771	0.6135	2.3673	61.8833
1.5	632.8	0.0154	1.1254	0.6318	3.0395	70.0372
1.5	632.8	0.0212	1.3723	0.6383	0.9531	63.7781
1.5	632.8	0.0262	1.5031	0.6526	0.4377	56.9339
1.5	632.8	0.033	2.0618	0.6715	0.5257	61.9544
2	632.8	0.0115	0.9056	0.5806	3.0419	75.7062
2	632.8	0.0154	1.2409	0.6452	0.9779	79.5975
2	632.8	0.0215	1.6768	0.6469	0.7388	77.2521
2	632.8	0.0263	2.0257	0.6687	0.328	76.6949
2	632.8	0.0326	2.5947	0.6659	0.3191	79.2717
1	632.8	0.0112	0.5451	0.606	4.2796	44.386
1	632.8	0.0163	0.5512	0.6606	0.4803	33.3378
1	632.8	0.0223	0.9292	0.6437	1.244	40.4252
1	632.8	0.026	1.3146	0.6497	1.9	48.6617
1	632.8	0.032	1.4742	0.6672	0.8952	45.1722
1	632.8	0.0113	0.4425	0.65	1.4406	37.7146
1	632.8	0.0147	0.6456	0.6277	1.9078	42.0109
1	632.8	0.0216	0.8464	0.641	0.769	38.4163
1	632.8	0.0261	1.028	0.6415	0.5399	38.8455
1	632.8	0.033	1.308	0.649	0.5302	39.1049
1.5	632.8	0.012	0.7644	0.6264	2.0638	61.6356
1.5	632.8	0.0154	0.9666	0.6266	1.8205	60.945
1.5	632.8	0.0212	1.1803	0.6474	0.1001	55.5743
1.5	632.8	0.0262	1.5031	0.6682	0.2771	57.0944
1.5	632.8	0.033	2.052	0.6589	0.537	61.6453
2	632.8	0.0115	0.9279	0.6299	1.9725	78.712
2	632.8	0.0154	1.2147	0.6376	0.6811	78.1943
2	632.8	0.0215	1.6672	0.6364	1.0196	76.525
2	632.8	0.0263	2.1772	0.6559	0.6969	82.0859
2	632.8	0.0326	2.4829	0.6608	0.256	75.9061
1.5	780	0.0111	0.4543	0.4802	3.2059	37.7187
1.5	780	0.0207	0.7076	0.5285	0.237	33.9446
1.5	780	0.0317	0.9299	0.4134	0	29.3347
1.5	780	0.0418	1.4139	0.5535	0.1116	33.7144
1.5	780	0.0502	1.6127	0.5165	0	32.1261
1.5	780	0.0111	0.4832	0.5041	2.9423	40.5882
1.5	780	0.0207	0.7407	0.5274	0.625	35.1561
1.5	780	0.0317	1.0429	0.4903	0	32.8979
1.5	780	0.0418	1.4394	0.5386	0.1454	34.2909
1.5	780	0.0502	1.6158	0.5004	0	32.1869

Intralipid one Integr. Sphere

concentration	wavelength	thickness	opt. thickness	g	mu_a	mu_s
[%]	[nm]	[cm]	[-]	[-]	[cm-1]	[cm-1]
1	632.8	0.0112	0.5231	0.67	4.5329	42.1739
1	632.8	0.0163	0.5295	0.7209	0.6951	31.7924
1	632.8	0.0223	0.8444	0.6705	1.4236	36.441
1	632.8	0.026	1.3022	0.7135	1.9189	48.1652
1	632.8	0.032	2.0081	0.7053	2.6374	60.1171
1	632.8	0.0113	0.4584	0.6882	2.7623	37.8011
1	632.8	0.0147	0.6623	0.6611	3.0092	42.0478
1	632.8	0.0216	0.8104	0.6802	1.2076	36.3103
1	632.8	0.0261	1.0484	0.6766	1.2774	38.8925
1	632.8	0.033	1.3074	0.6727	1.0396	38.5792
1.5	632.8	0.012	0.8258	0.6586	4.3903	64.4303
1.5	632.8	0.0154	1.4571	0.6359	7.2785	87.3386
1.5	632.8	0.0212	1.259	0.6622	0.9299	58.4579
1.5	632.8	0.0262	1.537	0.6776	0.9273	57.7358
1.5	632.8	0.033	1.9835	0.6702	1.091	59.0151
2	632.8	0.0115	0.8423	0.6683	2.1909	71.0513
2	632.8	0.0154	1.1935	0.652	2.1084	75.3944
2	632.8	0.0215	1.6897	0.6746	1.323	77.27
2	632.8	0.0263	2.0232	0.6512	1.0549	75.8729
2	632.8	0.0326	2.5175	0.6756	0.5937	76.6302
1	632.8	0.0112	0.5177	0.6643	3.7816	42.4422
1	632.8	0.0163	0.5875	0.7019	1.8116	34.2338
1	632.8	0.0223	0.9243	0.6845	1.9309	39.5198
1	632.8	0.026	1.3165	0.6849	2.2971	48.337
1	632.8	0.032	1.5294	0.6954	1.5442	46.2503
1	632.8	0.0113	0.4584	0.6808	2.9213	37.6456
1	632.8	0.0147	0.6154	0.6723	2.0868	39.7739
1	632.8	0.0216	0.839	0.6823	1.324	37.5172
1	632.8	0.0261	1.0813	0.677	1.3941	40.0356
1	632.8	0.033	1.2925	0.671	0.8678	38.2992
1.5	632.8	0.012	0.7931	0.6847	3.6114	62.478
1.5	632.8	0.0154	1.0949	0.6623	3.6856	67.4112
1.5	632.8	0.0212	1.3253	0.6608	1.3886	61.1257
1.5	632.8	0.0262	1.6118	0.6588	1.333	60.1877
1.5	632.8	0.033	2.086	0.6826	0.9415	62.2702
2	632.8	0.0115	0.884	0.6641	2.2768	74.5906
2	632.8	0.0154	1.2429	0.6794	1.9967	78.7138
2	632.8	0.0215	1.6752	0.6542	1.5075	76.4088
2	632.8	0.0263	2.0327	0.6816	0.8404	76.4494
2	632.8	0.0326	2.5295	0.6723	0.6719	76.9195
1.5	780	0.0111	0.4645	0.5393	3.9239	37.9197
1.5	780	0.0207	0.7405	0.568	0.8722	34.9011
1.5	780	0.0317	0.9396	0.4892	0	29.6402
1.5	780	0.0418	1.368	0.5515	0.2055	32.5218
1.5	780	0.0502	1.5462	0.5678	0.0188	30.7818
1.5	780	0.0111	0.5956	0.4903	8.3513	45.3027
1.5	780	0.0207	0.7415	0.5597	1.1712	34.6487
1.5	780	0.0317	0.9795	0.5626	0	30.8985
1.5	780	0.0418	1.4128	0.5589	0.2609	33.5376
1.5	780	0.0502	1.5909	0.5607	0.113	31.5777

concentration	wavelength	thickness	opt. thickness	g	mu_a	mu_s
[%]	[nm]	[cm]	[-]	[-]	[cm-1]	[cm-1]
0.23	780	0.0115	0.7607	0.7965	6.9569	59.1945
0.23	780	0.0212	1.1711	0.85	1.7417	53.5001
0.23	780	0.0314	1.8572	0.8768	0.5812	58.5665
0.23	780	0.0411	2.5757	0.882	0.5854	62.0826
0.71	780	0.0116	1.8827	0.8692	1.1615	161.1414
0.23	780	0.0115	0.7796	0.7748	8.3968	59.3986
0.23	780	0.0212	1.1418	0.8525	1.1784	52.6789
0.23	780	0.0314	1.8085	0.8606	0.7323	56.8618
0.23	780	0.0411	2.5326	0.8695	0.7311	60.8903
0.71	780	0.0116	1.7606	0.8886	0.1464	151.6295
0.71	780	0.0211	3.3088	0.8888	0.0747	156.739
0.71	632.8	0.011	2.6098	0.8921	1.1506	236.1039
0.71	632.8	0.0211	3.8056	0.9009	0.0911	180.2685
0.05	632.8	0.0138	0.2633	0.8248	0.8614	18.2198
0.05	632.8	0.0251	0.557	0.8834	0.3568	21.8364
0.05	632.8	0.0455	0.9767	0.8797	0.2847	21.1804
0.05	632.8	0.0455	0.9767	0.8797	0.2847	21.1804
0.05	632.8	0.0538	1.1105	0.8714	0.4352	20.2053
0.1	632.8	0.0134	0.4251	0.8305	1.2395	30.4817
0.1	632.8	0.0254	0.9317	0.877	0.5243	36.1576
0.1	632.8	0.0458	1.247	0.8693	0.4665	26.76
0.1	632.8	0.0533	1.3333	0.8614	0.6538	24.3618
0.167	632.8	0.0138	0.8076	0.8742	0.824	57.7004
0.167	632.8	0.0251	1.6345	0.8915	0.6093	64.5088
0.167	632.8	0.0331	1.8922	0.8917	0.4993	56.6657
0.167	632.8	0.0454	2.9374	0.9036	0.1346	64.5651
0.167	632.8	0.0526	3.1069	0.9039	0.2292	58.8376
0.227	632.8	0.0136	0.9568	0.8704	1.0468	69.3047
0.227	632.8	0.0245	2.4486	0.8969	0.4045	99.5404
0.227	632.8	0.0314	2.3852	0.8966	0.3875	75.5755
0.227	632.8	0.0454	4.0426	0.904	0.0625	88.982
0.227	632.8	0.0538	4.1313	0.9042	0.0623	76.7282
0.417	632.8	0.0137	1.8658	0.8939	0.8753	135.3146
0.417	632.8	0.0251	3.9687	0.9057	0.0559	158.0591
0.417	632.8	0.0333	4.3808	0.9049	0.0363	131.5193
0.417	632.8	0.0538	7.2769	0.908	0.0169	135.2408
0.05	632.8	0.0138	0.2574	0.8368	0.9503	17.7024
0.05	632.8	0.0455	0.9475	0.8882	0.152	20.6721
0.05	632.8	0.0455	0.9475	0.8882	0.1519	20.6722
0.05	632.8	0.0538	1.1029	0.8669	0.452	20.0475
0.1	632.8	0.0134	0.3965	0.8497	1.2501	28.3358
0.1	632.8	0.0254	0.896	0.8715	0.3726	34.9049
0.1	632.8	0.0326	0.7534	0.788	0.8768	22.2349
0.1	632.8	0.0458	1.2911	0.8581	0.6364	27.5538
0.1	632.8	0.0533	1.2078	0.8579	0.4293	22.2306
0.167	632.8	0.0138	0.7753	0.859	1.2523	54.9313
0.167	632.8	0.0251	1.5792	0.8838	0.5597	62.3585
0.167	632.8	0.0331	1.8313	0.8873	0.4376	54.8876
0.167	632.8	0.0454	2.9362	0.9061	0.0369	64.637
0.167	632.8	0.0526	3.0716	0.9004	0.2307	58.1652
0.227	632.8	0.0136	0.9686	0.8569	1.501	69.7185
0.227	632.8	0.0245	2.4093	0.8583	0.878	97.4628
0.227	632.8	0.0314	2.482	0.8869	0.5287	78.5159
0.227	632.8	0.0454	3.9723	0.8965	0.1082	87.3867
0.227	632.8	0.0538	4.1717	0.8969	0.1043	77.4363
0.417	632.8	0.0137	1.7634	0.8867	0.7851	127.9303
0.417	632.8	0.0251	3.9136	0.9	0.047	155.8733
0.417	632.8	0.0333	4.2944	0.9051	0.0023	128.9583
0.417	632.8	0.0538	7.308	0.9046	0.0173	135.8185
0.71	632.8	0.011	2.6774	0.9059	0.561	242.8365

concentration	wavelength	thickness	opt. thickness	g	mu_a	mu_s
[%]	[nm]	[cm]	[-]	[-]	[cm-1]	cm[-1]
0.23	780	0.0115	0.7607	0.8825	6.8475	59.3039
0.23	780	0.0212	1.1623	0.8953	2.4499	52.3774
0.23	780	0.0314	1.8149	0.8966	0.9653	56.8326
0.23	780	0.0411	2.4968	0.8941	1.0395	59.7099
0.71	780	0.0116	1.9345	0.908	1.0808	165.684
0.71	780	0.0211	3.6503	0.8975	0.476	172.5246
0.71	780	0.0314	6.0139	0.898	0.2615	191.2628
0.71	780	0.0412	7.3473	0.7126	3.5568	174.7759
0.23	780	0.0115	0.8418	0.8504	10.4155	62.7834
0.23	780	0.0212	1.1848	0.8803	3.1361	52.7507
0.23	780	0.0314	1.8215	0.8915	1.2272	56.7831
0.23	780	0.0411	2.4373	0.8923	0.7768	58.5256
0.71	780	0.0116	2.3605	0.8981	2.4499	201.0394
0.71	780	0.0211	3.4832	0.9043	0.3169	164.7655
0.71	780	0.0314	5.72	0.8947	0.2935	181.8737
0.71	780	0.0412	7.3633	0.9	0.0146	178.7053
0.71	632.8	0.011	2.7365	0.922	2.124	246.6451
0.71	632.8	0.0211	3.9898	0.9229	0.1197	188.9694
0.71	632.8	0.0314	8.1972	0.9155	0.1124	260.9444
0.71	632.8	0.0412	10.451	0.9172	0.0458	253.6187
0.05	632.8	0.0138	0.2735	0.9428	2.0447	17.7724
0.05	632.8	0.0251	0.5686	0.9062	1.965	20.6875
0.05	632.8	0.0455	0.9887	0.9307	0.8303	20.8996
0.05	632.8	0.0455	0.9887	0.9307	0.8303	20.8996
0.05	632.8	0.0538	1.0792	0.9386	0.7646	19.2944
0.1	632.8	0.0134	0.3995	0.9404	1.3671	28.4498
0.1	632.8	0.0254	0.9592	0.9066	1.8122	35.9529
0.1	632.8	0.0326	0.7398	0.9017	1.7604	20.9334
0.1	632.8	0.0458	1.2298	0.9015	1.131	25.7202
0.1	632.8	0.0533	1.2837	0.9047	1.0685	23.0159
0.167	632.8	0.0138	0.8489	0.9256	2.8582	58.6559
0.167	632.8	0.0251	1.7101	0.9196	1.419	66.712
0.167	632.8	0.0331	1.9573	0.9166	1.0654	58.0684
0.167	632.8	0.0454	2.9638	0.9152	0.6203	64.6613
0.167	632.8	0.0526	3.2687	0.9162	0.6825	61.4597
0.227	632.8	0.0136	0.9512	0.9223	1.9321	68.0062
0.227	632.8	0.0245	2.4896	0.9054	1.4438	100.1717
0.227	632.8	0.0314	2.5083	0.9129	0.9495	78.9331
0.227	632.8	0.0454	4.0549	0.9121	0.3887	88.927
0.227	632.8	0.0538	4.3351	0.9071	0.4399	80.1373
0.417	632.8	0.0137	1.9061	0.9191	2.0853	137.0479
0.417	632.8	0.0251	4.1519	0.912	0.708	164.7068
0.417	632.8	0.0333	4.4987	0.9119	0.5347	134.5624
0.417	632.8	0.0456	6.7771	0.9111	0.2324	148.388
0.417	632.8	0.0538	7.3916	0.9144	0.2136	137.1763
0.05	632.8	0.0138	0.2952	0.9087	3.2214	18.1677
0.05	632.8	0.0251	0.6266	0.9106	2.2923	22.6715
0.05	632.8	0.0455	0.9871	0.9277	0.8442	20.8506
0.05	632.8	0.0455	0.9871	0.9277	0.8442	20.8506
0.05	632.8	0.0538	1.1264	0.9147	0.8805	20.0559
0.1	632.8	0.0134	0.3847	0.924	1.6212	27.0898
0.1	632.8	0.0254	0.9126	0.9019	0.8514	35.0764
0.1	632.8	0.0326	0.7358	0.9444	0	22.5696
0.1	632.8	0.0458	1.2716	0.9099	1.08	26.6843
0.1	632.8	0.0533	1.3484	0.9066	1.1363	24.1625
0.167	632.8	0.0138	0.8021	0.9307	2.1855	55.9357
0.167	632.8	0.0251	1.7024	0.9181	1.6635	66.1605
0.167	632.8	0.0331	1.9271	0.9157	1.1355	57.0858
0.167	632.8	0.0454	2.9627	0.9233	0.4265	64.8316
0.167	632.8	0.0526	3.171	0.9154	0.6492	59.6358
0.227	632.8	0.0136	1.0555	0.9078	4.1401	73.4668
0.227	632.8	0.0245	2.4959	0.9102	1.1901	100.6844

concentration	wavelength	thickness	opt. thickness	g	mu_a	mu_s
0.227	632.8	0.0314	2.458	0.9081	1.1324	77.147
0.227	632.8	0.0454	4.0005	0.9122	0.2773	87.8399
0.227	632.8	0.0538	4.31	0.9121	0.2804	79.8305
0.417	632.8	0.0137	1.8956	0.9175	2.5488	135.816
0.417	632.8	0.0251	4.0544	0.9143	0.5891	160.9394
0.417	632.8	0.0333	4.3137	0.9118	0.5457	128.995
0.417	632.8	0.0456	6.741	0.9085	0.3593	147.4699
0.417	632.8	0.0538	7.298	0.9103	0.257	135.3927
0.71	632.8	0.011	2.7841	0.9166	2.3915	250.7124
0.71	632.8	0.0211	3.9613	0.9144	0.6541	187.0872
0.71	632.8	0.0314	7.8999	0.9149	0.0597	251.5305
0.71	632.8	0.0412	10.3247	0.916	0.0854	250.5138